

Finding the superior mode basis for mode-division multiplexing: a comparison of spatial modes in air-core fiber

Hongya Wang,^{a,b} Jianzhou Ai,^{a,b} Zelin Ma,^c Siddharth Ramachandran,^c and Jian Wang^{a,b,*}

^aHuazhong University of Science and Technology, Wuhan National Laboratory for Optoelectronics and School of Optical and Electronic Information, Wuhan, China

^bOptics Valley Laboratory, Wuhan, China

^cBoston University, Boston, Massachusetts, United States

Abstract. Diverse spatial mode bases can be exploited in mode-division multiplexing (MDM) to sustain the capacity growth in fiber-optic communications, such as linearly polarized (LP) modes, vector modes, LP orbital angular momentum (LP-OAM) modes, and circularly polarized OAM (CP-OAM) modes. Nevertheless, which kind of mode bases is more appropriate to be utilized in fiber still remains unclear. Here, we aim to find the superior mode basis in MDM fiber-optic communications via a system-level comparison in air-core fiber (ACF). We first investigate the walk-off effect of four spatial mode bases over 1-km ACF, where LP and LP-OAM modes show intrinsic mode walk-off, while it is negligible for vector and CP-OAM modes. We then study the mode coupling effect of degenerate vector and CP-OAM modes over 1-km ACF under fiber perturbations, where degenerate even and odd vector modes suffer severe mode cross talk, while negligible for high-order degenerate CP-OAM modes based on the laws of angular momentum conservation. Moreover, we comprehensively evaluate the system-level performance for data-carrying single-channel and two-channel MDM transmission with different spatial mode bases under various kinds of fiber perturbations (bending, twisting, pressing, winding, and out-of-plane moving). The obtained results indicate that the CP-OAM mode basis shows superiority compared to other mode bases in MDM fiber-optic communications without using multiple-input multiple-output digital signal processing. Our findings may pave the way for robust short-reach MDM optical interconnects for data centers and high-performance computing.

Keywords: fiber-optic communications; mode-division multiplexing; spatial modes; linearly polarized modes; vector modes; linearly polarized orbital angular momentum modes; circularly polarized orbital angular momentum modes; air-core fiber; fiber perturbations.

Received Mar. 4, 2023; revised manuscript received Jul. 2, 2023; accepted for publication Jul. 17, 2023; published online Sep. 1, 2023.

© The Authors. Published by SPIE and CLP under a Creative Commons Attribution 4.0 International License. Distribution or reproduction of this work in whole or in part requires full attribution of the original publication, including its DOI.

[DOI: [10.11117/1.AP.5.5.056003](https://doi.org/10.11117/1.AP.5.5.056003)]

1 Introduction

With the rising demand for communication speed and capacity due to the exponential growth of information traffic, mode-division multiplexing (MDM), a subset of space-division multiplexing (SDM), has been attracting extensive interest in recent years.^{1–3} MDM using multiple spatial modes can form a couple of

information channels carrying independent data streams, which is capable of remarkably increasing the transmission capacity density and the spectral efficiency in a single fiber.^{4–6} In general, there are many sorts of mode bases that are applicable in MDM-based fiber-optic transmission systems, for instance, linearly polarized (LP) modes,^{4–9} vector modes,^{10–14} LP and circularly polarized (CP) orbital angular momentum (OAM) modes.^{15–33}

Very recently, MDM has been widely studied in many sorts of fibers with cylindrical symmetry, such as multimode fibers

*Address all correspondence to Jian Wang, jwang@hust.edu.cn

(MMFs)^{6,29–32} and few-mode fibers (FMFs).^{4,7,8,13,14,16,17,19,33} Remarkably, in most cases, several simultaneously propagating spatial modes would inevitably mix in the presence of perturbations. Thus multiple-input multiple-output (MIMO) digital signal processing (DSP) is essential to compensate for the mixing-induced cross talk for recovering data streams from multiple information channels. It is worth noting that MIMO-DSP scales in complexity with N^2 , where N is the number of modes, which results in a continuous growth in hardware cost and power consumption.³ Even though the mode mixing can be alleviated in some specially designed ring-core fibers (RCFs)^{22,23,26–28} with cylindrical symmetry, e.g., for different mode groups, MIMO-DSP is still highly desired within each mode group to take full advantage of all spatial modes to efficiently increase the channel number as many as possible.^{23,26,27} Furthermore, given that the complexity of MIMO-DSP also increases with the differential group delay (DGD) among channels, low DGD among different modes is needed, while correspondingly mode mixing may get worse. Therefore, it is contradictory between increasing the information channel number and simultaneously decreasing the cost of MIMO-DSP in MMFs, FMFs, and RCFs.

To simultaneously make full use of all spatial modes, increase the channel number, and reduce the intermodal coupling, MIMO-free MDM systems have been proposed and developed.^{21,22,25} One alternative proposal is to apply elliptical-core fibers (ECFs) or photonic crystal fibers (PCFs), where all fiber eigenmodes are fully lifted or separated so that each fiber eigenmode can be used as an individual information channel.^{12,34–40} However, these ECFs and PCFs with cylindrical symmetry broken present a great challenge in high-performance fiber manufacturing. Moreover, it is also difficult to flexibly control (e.g., multiplex and demultiplex) these fiber eigenmodes with cylindrical symmetry broken in ECFs and PCFs. Another impactful way to form an MDM system without MIMO-DSP is to employ OAM modes in an air-core fiber (ACF).^{21,25,41–44} Note that the ACF retains its cylindrical symmetry, while the degeneracy between EH/HE modes in the same mode group is lifted due to the high-contrast index of the ACF.^{21,25,41–44}

Notably, diverse spatial mode bases, such as LP modes, linearly polarized orbital angular momentum (LP-OAM) modes, vector modes, and circularly polarized orbital angular momentum (CP-OAM) modes, have been successfully demonstrated in MDM fiber-optic communications, even for cylindrically symmetric fibers. However, to the best of our knowledge, there has been limited research on their detailed comparison, especially from a system-level point of view. In this scenario, a laudable goal would be to give a comprehensive comparison among different spatial mode bases and find the favorable one for MDM fiber-optic communication applications. Here we aim to search for the superior mode basis for MDM fiber-optic communications, particularly in ACF with cylindrical symmetry. We give a detailed system-level comparison through bit-error rate (BER) evaluation among all four spatial mode bases (LP modes, LP-OAM modes, vector modes, and CP-OAM modes). We find CP-OAM modes show impressive performance against fiber perturbations. These findings may help to optimize system performance with suitable spatial modes in MDM fiber-optic communications, especially for short-reach optical interconnects for data centers and high-performance computing applications that may deploy new fibers.

2 Concept, Principle, and Theory

The concept and principle of a comparison among different spatial mode bases for finding the superior one are illustrated in Fig. 1. Four kinds of spatial mode bases in cylindrically symmetric fiber, i.e., vector modes, LP modes, LP-OAM modes, and CP-OAM modes, are considered for comparison and later system-level experimental demonstration.

In the case of high-order vector modes, the electric fields of HE and EH modes can be described as

$$\text{HE}_{l+1,m}^{\text{odd}} = F_{l,m}(r)[\hat{x} \sin(l\phi) + \hat{y} \cos(l\phi)] \exp(i\beta_{\text{HE},z} \cdot z), \quad (1a)$$

$$\text{HE}_{l+1,m}^{\text{even}} = F_{l,m}(r)[\hat{x} \cos(l\phi) - \hat{y} \sin(l\phi)] \exp(i\beta_{\text{HE},z} \cdot z), \quad (1b)$$

$$\text{EH}_{l-1,m}^{\text{odd}} = F_{l,m}(r)[\hat{x} \sin(l\phi) - \hat{y} \cos(l\phi)] \exp(i\beta_{\text{EH},z} \cdot z), \quad (1c)$$

$$\text{EH}_{l-1,m}^{\text{even}} = F_{l,m}(r)[\hat{x} \cos(l\phi) + \hat{y} \sin(l\phi)] \exp(i\beta_{\text{EH},z} \cdot z), \quad (1d)$$

where the superscripts “odd” and “even” denote odd and even modes, respectively, the subscripts l ($l > 1$) and m stand for the azimuthal order and radial order, respectively, $F_{l,m}(r)$ is the electric field profile along the radial direction (r), (r, ϕ) are the cylindrical coordinates, \hat{x} and \hat{y} are the unit vectors along x and y directions in the Cartesian coordinates (x, y) , and $\beta_{\text{HE},z}$ and $\beta_{\text{EH},z}$ are the effective propagation constants of HE and EH modes along the z direction, respectively.

Remarkably, in cylindrically symmetric fiber, the four kinds of spatial mode bases (vector modes, LP modes, LP-OAM modes, and CP-OAM modes) can be deduced from each other. For instance, both LP modes and OAM modes can be synthesized from the linear combination of vector modes of the fiber.

In the case of high-order LP modes, the general relationship between LP modes and vector modes can be written as

$$\text{LP}_{l,m}^{x,\text{odd}} = \text{EH}_{l-1,m}^{\text{odd}} + \text{HE}_{l+1,m}^{\text{odd}}, \quad (2a)$$

$$\text{LP}_{l,m}^{x,\text{even}} = \text{EH}_{l-1,m}^{\text{even}} + \text{HE}_{l+1,m}^{\text{even}}, \quad (2b)$$

$$\text{LP}_{l,m}^{y,\text{even}} = \text{EH}_{l-1,m}^{\text{odd}} - \text{HE}_{l+1,m}^{\text{odd}}, \quad (2c)$$

$$\text{LP}_{l,m}^{y,\text{odd}} = \text{EH}_{l-1,m}^{\text{even}} - \text{HE}_{l+1,m}^{\text{even}}, \quad (2d)$$

where the superscripts x and y denote the x polarization and y polarization, respectively. In weakly guiding fiber where $\beta_{\text{HE},z} \approx \beta_{\text{EH},z} \approx \beta_z$, Eq. (2) can be expressed as

$$\text{LP}_{l,m}^{x,\text{odd}} = 2F_{l,m}(r)\hat{x} \sin(l\phi) \exp(i\beta_z \cdot z), \quad (3a)$$

$$\text{LP}_{l,m}^{x,\text{even}} = 2F_{l,m}(r)\hat{x} \cos(l\phi) \exp(i\beta_z \cdot z), \quad (3b)$$

$$\text{LP}_{l,m}^{y,\text{even}} = -2F_{l,m}(r)\hat{y} \cos(l\phi) \exp(i\beta_z \cdot z), \quad (3c)$$

$$\text{LP}_{l,m}^{y,\text{odd}} = 2F_{l,m}(r)\hat{y} \sin(l\phi) \exp(i\beta_z \cdot z). \quad (3d)$$

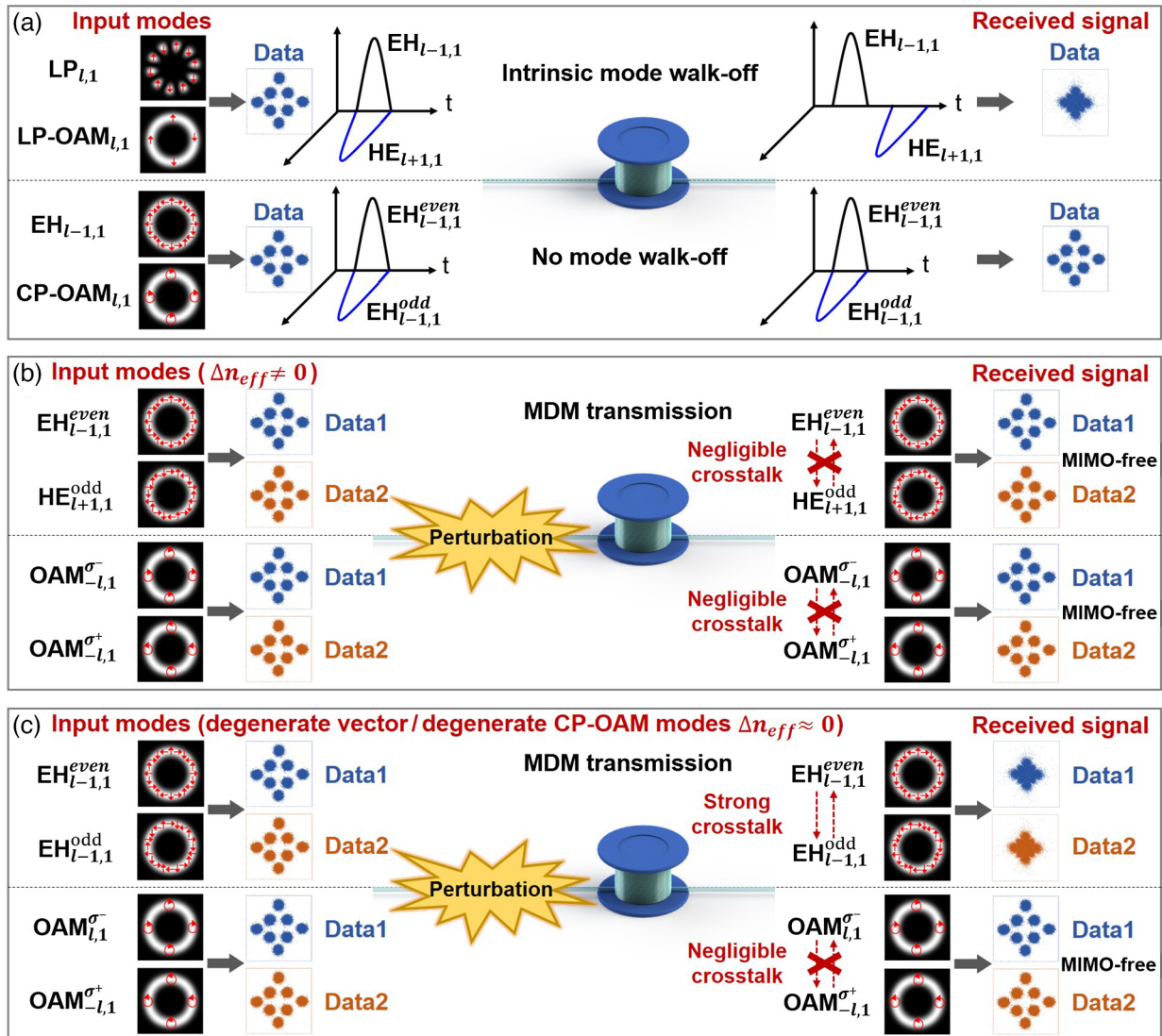


Fig. 1 Concept and principle of a comparison among different spatial mode bases (LP, LP-OAM, vector, and CP-OAM) in ACF. (a) Intrinsic mode walk-off for LP/LP-OAM modes and no mode walk-off for vector/CP-OAM modes. (b) Data-carrying MDM transmission using spatial modes with large Δn_{eff} (negligible cross talk and MIMO-free) under fiber perturbations. (c) Data-carrying MDM transmission using degenerate vector modes (strong cross talk) or degenerate CP-OAM modes (negligible cross talk and MIMO-free) under fiber perturbations.

From Eqs. (1) and (2), one can find that LP modes are composed of two different fiber vector modes, which have different propagation constants ($\beta_{HE,z} \neq \beta_{EH,z}$) in fiber with a relatively high-contrast index, such as ACF. When propagating along such fiber supporting nondegenerate HE and EH modes, the LP mode bases will suffer from the intrinsic walk-off effect after propagation even without any perturbation, as illustrated in Fig. 1(a).

In the case of high-order LP-OAM modes, they can be regarded as a superposition of two LP modes with a $\pm\pi/2$ phase difference (weakly guiding fiber) from the formula. In fact, LP-OAM modes are the linear combination of all four vector modes (even HE, odd HE, odd EH, and even EH) as follows:

$$\begin{aligned} OAM_{l,m}^x &= LP_{l,m}^{x,even} + iLP_{l,m}^{x,odd} = 2F_{l,m}(r)\hat{x}\exp(il\phi)\exp(i\beta_z \cdot z) \\ &= EH_{l-1,m}^{even} + HE_{l+1,m}^{even} + iEH_{l-1,m}^{odd} + iHE_{l+1,m}^{odd}, \end{aligned} \quad (4a)$$

$$\begin{aligned} OAM_{-l,m}^x &= LP_{l,m}^{x,even} - iLP_{l,m}^{x,odd} \\ &= 2F_{l,m}(r)\hat{x}\exp(-il\phi)\exp(i\beta_z \cdot z) \\ &= EH_{l-1,m}^{even} + HE_{l+1,m}^{even} - iEH_{l-1,m}^{odd} - iHE_{l+1,m}^{odd}, \end{aligned} \quad (4b)$$

$$\begin{aligned} OAM_{l,m}^y &= LP_{l,m}^{y,even} - iLP_{l,m}^{y,odd} \\ &= -2F_{l,m}(r)\hat{y}\exp(il\phi)\exp(i\beta_z \cdot z) \\ &= EH_{l-1,m}^{odd} - HE_{l+1,m}^{odd} - iEH_{l-1,m}^{even} + iHE_{l+1,m}^{even}, \end{aligned} \quad (4c)$$

$$\begin{aligned} OAM_{-l,m}^y &= LP_{l,m}^{y,even} + iLP_{l,m}^{y,odd} \\ &= -2F_{l,m}(r)\hat{y}\exp(-il\phi)\exp(i\beta_z \cdot z) \\ &= EH_{l-1,m}^{odd} - HE_{l+1,m}^{odd} + iEH_{l-1,m}^{even} - iHE_{l+1,m}^{even}, \end{aligned} \quad (4d)$$

where the azimuthal order l is also known as the topological charge of the OAM mode, and the radial order m is also the number of concentric rings in the intensity profile of the mode. β_z is for the weakly guiding fiber. Hence, a similar walk-off phenomenon would also occur for LP-OAM modes in ACF, as illustrated in Fig. 1(a).

In the case of high-order CP-OAM modes, the relationship between CP-OAM modes and vector modes can be expressed as

$$\begin{aligned} \text{OAM}_{l,m}^{\sigma^+} &= \text{HE}_{l+1,m}^{\text{even}} + i\text{HE}_{l+1,m}^{\text{odd}} \\ &= F_{l,m}(r) \begin{pmatrix} 1 \\ i \end{pmatrix} \exp(il\phi) \exp(i\beta_{\text{HE},z} \cdot z), \end{aligned} \quad (5a)$$

$$\begin{aligned} \text{OAM}_{-l,m}^{\sigma^-} &= \text{HE}_{l+1,m}^{\text{even}} - i\text{HE}_{l+1,m}^{\text{odd}} \\ &= F_{l,m}(r) \begin{pmatrix} 1 \\ -i \end{pmatrix} \exp(-il\phi) \exp(i\beta_{\text{HE},z} \cdot z), \end{aligned} \quad (5b)$$

$$\begin{aligned} \text{OAM}_{l,m}^{\sigma^-} &= \text{EH}_{l-1,m}^{\text{even}} + i\text{EH}_{l-1,m}^{\text{odd}} \\ &= F_{l,m}(r) \begin{pmatrix} 1 \\ -i \end{pmatrix} \exp(il\phi) \exp(i\beta_{\text{EH},z} \cdot z), \end{aligned} \quad (5c)$$

$$\begin{aligned} \text{OAM}_{-l,m}^{\sigma^+} &= \text{EH}_{l-1,m}^{\text{even}} - i\text{EH}_{l-1,m}^{\text{odd}} \\ &= F_{l,m}(r) \begin{pmatrix} 1 \\ i \end{pmatrix} \exp(-il\phi) \exp(i\beta_{\text{EH},z} \cdot z), \end{aligned} \quad (5d)$$

where $\sigma^+ = \begin{pmatrix} 1 \\ i \end{pmatrix} = \hat{x} + i\hat{y}$ and $\sigma^- = \begin{pmatrix} 1 \\ -i \end{pmatrix} = \hat{x} - i\hat{y}$ denote left- and right-handed circular polarizations, respectively. From Eqs. (1) and (5), one can find that CP-OAM modes can be regarded as a superposition of even and odd HE or EH modes with a $\pm\pi/2$ phase difference. In cylindrically symmetric fiber with a relatively high-contrast index, although the HE and EH modes are nondegenerate ($\beta_{\text{HE},z} \neq \beta_{\text{EH},z}$), the even and odd HE modes, having the same propagation constant ($\beta_{\text{HE},z}$), are degenerate with each other. Actually, the vector fields of the even and odd HE modes are the same upon proper angular rotation. Similarly, the even and odd EH modes are also degenerate ($\beta_{\text{EH},z}$). Consequently, there is no intrinsic walk-off effect for vector mode bases and CP-OAM mode bases when propagating along an idea fiber without perturbation, as shown in Fig. 1(a).

Remarkably, fiber perturbations are inevitable in practical deployment of optical fibers, such as bending, twisting, pressing, winding, moving, and various environmental disturbances, which may cause coupling between spatial modes. In general, the power coupling coefficient between any two spatial modes (E_u and E_v) under the fiber perturbation can be expressed as^{41,45}

$$P_{u,v} = \frac{\omega^2}{c^2} \Phi(\beta_u - \beta_v) \cdot \left(\iint E_u^* T_{\text{pert}} E_v r dr d\phi \right)^2, \quad (6)$$

where the perturbation acting on the fiber can be decomposed into the transverse perturbation $T_{\text{pert}}(r, \phi)$ and longitudinal perturbation $L_{\text{pert}}(z)$, $\Phi(\beta_u - \beta_v)$ is the spatial power spectrum of the autocorrelation of $L_{\text{pert}}(z)$, $\beta_u = 2\pi n_{\text{eff},u}/\lambda$ and $\beta_v = 2\pi n_{\text{eff},v}/\lambda$ are the longitudinal propagation constants, $n_{\text{eff},u}$ and $n_{\text{eff},v}$ are the mode effective refractive indices, (r, ϕ) are the transverse

coordinates, E_u and E_v are the normalized electric fields of two spatial modes, ω is the frequency, λ is the wavelength, and c is the light velocity in vacuum. $\Phi(\beta_u - \beta_v)$ can be expressed as

$$\Phi(\beta_u - \beta_v) = \sqrt{\pi} \sigma_{\text{rms}}^2 L_c \exp\{-[L_c(\beta_u - \beta_v)/2]^2\}, \quad (7)$$

where σ_{rms} and L_c are the root-mean-square deviation and correlation length of $L_{\text{pert}}(z)$, respectively. Note that the transverse perturbation $T_{\text{pert}}(r, \phi)$ can be expanded as

$$T_{\text{pert}}(r, \phi) = \sum_{n=-\infty}^{\infty} t_n(r) \exp(in\phi), \quad (8)$$

where $t_n(r)$ is the coefficient of the series expansion term (angular momentum component). Taking OAM modes ($\exp(il_u\phi)$, $\exp(il_v\phi)$) as an example, Eq. (6) can be written as

$$\begin{aligned} P_{u,v} &\propto \exp\{-[L_c(\beta_u - \beta_v)/2]^2\} \\ &\cdot \left\{ \sum_{n=-\infty}^{\infty} t_n \int_0^{2\pi} \exp[i(l_v - l_u + n)\phi] d\phi \right\}^2. \end{aligned} \quad (9)$$

Intuitively, from the first term in Eq. (9), the mode coupling is maximized for degenerate modes when $\beta_u = \beta_v$. It also implies that the mode coupling can be effectively reduced by increasing the propagation constant difference ($\Delta\beta = \beta_u - \beta_v$) or the mode effective refractive index difference ($\Delta n_{\text{eff}} = n_{\text{eff},u} - n_{\text{eff},v}$), which is achievable with proper fiber structure design. For the ACF in this work, the high-contrast-index design enables effective mode separation not only for modes in different mode groups ($\Delta n_{\text{eff}} > 1 \times 10^{-3}$) but also for high-order HE and EH modes in each mode group ($\Delta n_{\text{eff}} > 0.5 \times 10^{-4}$), leading to weak mode coupling, as illustrated in Fig. 1(b). From the second term in Eq. (9), when $l_v - l_u + n \neq 0$, the integral becomes zero and there is no mode coupling; when $l_v - l_u + n = 0$, the nonzero integral value contributes to the mode coupling. Hence, the available angular momentum component and its coefficient of the transverse perturbation have an impact on the mode coupling. Particularly, even for the degenerate modes with the same propagation constant and mode effective refractive index, such as $\text{OAM}_{l,m}^{\sigma^+}$ and $\text{OAM}_{-l,m}^{\sigma^-}$ or $\text{OAM}_{l,m}^{\sigma^-}$ and $\text{OAM}_{-l,m}^{\sigma^+}$, the mode coupling can be still negligible if the transverse perturbation does not contain sufficient angular momentum component to meet the condition of $l_v - l_u + n = 0$. This is actually possible, especially for high-order CP-OAM modes with the large value of l . The mode coupling between $\text{OAM}_{l,m}^{\sigma^+}$ and $\text{OAM}_{-l,m}^{\sigma^-}$ or between $\text{OAM}_{l,m}^{\sigma^-}$ and $\text{OAM}_{-l,m}^{\sigma^+}$ requires a transverse perturbation component of $n = 2|l|$, which is not easy to achieve for large $|l|$. It indicates the distinct mode stability property of high-order CP-OAM modes and the underlying mechanism rely on the laws of angular momentum conservation, even in the case of fiber perturbations.

Among various fiber perturbations, moving or lifting the fiber out of the plane (i.e., out-of-plane fiber movement) is of great interest, since it introduces an extra Pancharatnam–Berry phase, also known as the geometric phase.^{43,44} It is associated with the topological nature, which is different from the conventional propagation dynamic phase dependent on the fiber length. For single-mode fiber (SMF) configured in an out-of-

plane route with circular polarization input light, the output light beam acquires the geometric phase as^{46,47}

$$\Phi_{\text{gp}}(C) = -\sigma \cdot \Omega(C), \quad (10)$$

where σ is the handedness of the circular polarization of input light, C denotes the out-of-plane path contour, and $\Omega(C)$ represents the solid angle in momentum space spanned by the fiber's closed path in this space.

For fibers supporting high-order modes, e.g., ACF in this work, the interesting geometric phase phenomenon also exists, and the geometric phase is extended to be related to both SAM (σ) and OAM (l) carried by light beams, which can be written as⁴⁸

$$\Phi_{\text{gp}}(C) = -(\sigma + l) \cdot \Omega(C). \quad (11)$$

For high-order CP-OAM modes passing through the perturbed fiber, the perturbed output modes adding the extra geometric phase can be expressed as

$$\overline{\text{OAM}_{l,m}^{\sigma^+}} = \text{OAM}_{l,m}^{\sigma^+} \cdot \exp(i\Phi_{\text{gp}1}), \quad (12a)$$

$$\overline{\text{OAM}_{-l,m}^{\sigma^-}} = \text{OAM}_{-l,m}^{\sigma^-} \cdot \exp(-i\Phi_{\text{gp}1}), \quad (12b)$$

$$\overline{\text{OAM}_{l,m}^{\sigma^-}} = \text{OAM}_{l,m}^{\sigma^-} \cdot \exp(i\Phi_{\text{gp}2}), \quad (12c)$$

$$\overline{\text{OAM}_{-l,m}^{\sigma^+}} = \text{OAM}_{-l,m}^{\sigma^+} \cdot \exp(-i\Phi_{\text{gp}2}), \quad (12d)$$

where $\Phi_{\text{gp}1} = -(\sigma + l) \cdot \Omega$ and $\Phi_{\text{gp}2} = -(l - \sigma) \cdot \Omega$.

For high-order vector modes (formed by the linear combination of CP-OAM modes) passing through the perturbed fiber, the perturbed output modes can be regarded as the linear combination of perturbed CP-OAM modes expressed as

$$\begin{aligned} \overline{\text{HE}_{l+1,m}^{\text{even}}} &= \frac{1}{2} (\overline{\text{OAM}_{l,m}^{\sigma^+}} + \overline{\text{OAM}_{-l,m}^{\sigma^-}}) \\ &= \cos \Phi_{\text{gp}1} \cdot \text{HE}_{l+1,m}^{\text{even}} - \sin \Phi_{\text{gp}1} \cdot \text{HE}_{l+1,m}^{\text{odd}}, \end{aligned} \quad (13a)$$

$$\begin{aligned} \overline{\text{HE}_{l+1,m}^{\text{odd}}} &= \frac{1}{2i} (\overline{\text{OAM}_{l,m}^{\sigma^+}} - \overline{\text{OAM}_{-l,m}^{\sigma^-}}) \\ &= \cos \Phi_{\text{gp}1} \cdot \text{HE}_{l+1,m}^{\text{odd}} + \sin \Phi_{\text{gp}1} \cdot \text{HE}_{l+1,m}^{\text{even}}, \end{aligned} \quad (13b)$$

$$\begin{aligned} \overline{\text{EH}_{l-1,m}^{\text{even}}} &= \frac{1}{2} (\overline{\text{OAM}_{l,m}^{\sigma^-}} + \overline{\text{OAM}_{-l,m}^{\sigma^+}}) \\ &= \cos \Phi_{\text{gp}2} \cdot \text{EH}_{l-1,m}^{\text{even}} - \sin \Phi_{\text{gp}2} \cdot \text{EH}_{l-1,m}^{\text{odd}}, \end{aligned} \quad (13c)$$

$$\begin{aligned} \overline{\text{EH}_{l-1,m}^{\text{odd}}} &= \frac{1}{2i} (\overline{\text{OAM}_{l,m}^{\sigma^-}} - \overline{\text{OAM}_{-l,m}^{\sigma^+}}) \\ &= \cos \Phi_{\text{gp}2} \cdot \text{EH}_{l-1,m}^{\text{odd}} + \sin \Phi_{\text{gp}2} \cdot \text{EH}_{l-1,m}^{\text{even}}. \end{aligned} \quad (13d)$$

From Eqs. (12) and (13), one can clearly see that the out-of-plane fiber movement only introduces extra geometric phase to

the CP-OAM modes themselves without leading to mode coupling, as depicted in Fig. 1(c). In contrast, such an out-of-plane fiber movement causes significant mode coupling between degenerate even and odd vector modes ($\text{HE}_{l+1,m}^{\text{even}}$ and $\text{HE}_{l+1,m}^{\text{odd}}$ or $\text{EH}_{l-1,m}^{\text{even}}$ and $\text{EH}_{l-1,m}^{\text{odd}}$), as shown in Fig. 1(c).

From a system-level point of view, when carrying data information on each spatial mode for MDM fiber-optic communications, the walk-off effect and perturbation-induced mode coupling phenomenon can significantly degrade the signal quality and resultant system performance. As shown in Fig. 1(a), for LP and LP-OAM mode bases, the intrinsic walk-off effect can cause a distorted mode profile at the receiver, and the transmitted signal spreads temporally even for a single-channel transmission through an ideal fiber without any perturbation. For vector and CP-OAM mode bases, there is no walk-off effect and no signal spreading for a single-channel transmission. As shown in Fig. 1(b), for modes with a large mode effective refractive index difference (Δn_{eff}), e.g., high-order HE and EH modes, $\text{OAM}_{l,m}^{\sigma^+}/\text{OAM}_{-l,m}^{\sigma^-}$ and $\text{OAM}_{l,m}^{\sigma^-}/\text{OAM}_{-l,m}^{\sigma^+}$ modes, and OAM modes with different $|l|$, the mode coupling is suppressed, and MIMO-free data-carrying MDM transmission using these modes is available. As shown in Fig. 1(c), for degenerate even and odd vector modes in the vector mode basis, e.g., $\text{HE}_{l+1,m}^{\text{even}}$ and $\text{HE}_{l+1,m}^{\text{odd}}$, $\text{EH}_{l-1,m}^{\text{even}}$ and $\text{EH}_{l-1,m}^{\text{odd}}$, the out-of-plane fiber movement can cause mode coupling by an extra geometric phase, and MIMO-DSP is desired to mitigate the mode cross talk for data-carrying MDM transmission using vector modes. For degenerate $\text{OAM}_{l,m}^{\sigma^+}$ and $\text{OAM}_{-l,m}^{\sigma^-}$ modes or degenerate $\text{OAM}_{l,m}^{\sigma^-}$ and $\text{OAM}_{-l,m}^{\sigma^+}$ modes in the CP-OAM mode basis, the mode coupling decreases with the increase of $|l|$ and is negligible for large $|l|$ owing to the angular momentum conservation condition, which is not easily satisfied, leading to MIMO-free data-carrying MDM transmission. Meanwhile, the CP-OAM mode basis is also stable with negligible mode coupling under the out-of-plane fiber movement. In the following proof-of-concept system-level experiments, we choose several kinds of perturbations (bending, twisting, pressing, winding, and moving) as representative examples. We first loosely prepare a fiber spool to release the stress and minimize perturbations, i.e., for approximation of fiber without perturbation. We employ an in-line polarization controller (PC) on the ACF and adjust it to emulate relatively complicated perturbations including pressing, twisting, and slight out-of-plane fiber movement. We manually lift the fiber out of plane (out-of-plane fiber movement) to introduce a significant geometric phase. We put weight on the fiber to add pressure. We also wind the fiber into small circles, which includes bending, slight twisting, and slight out-of-plane fiber movement.

3 Experimental Implementation

In the system-level experiments to find the superior mode basis for MDM fiber-optic communications, we employ a 1-km ACF and compressively compare the transmission performance of different spatial mode bases (vector modes, LP modes, LP-OAM modes, and CP-OAM modes). The designed and fabricated ACF features an air core at the fiber center, and the modes are confined within the ring-structure high-index region with the outer SiO₂ cladding. The air core also plays a role as the inner cladding with enhanced index contrast. The measured refractive index profile of the ACF is shown in Fig. 2(a). The radius of the air core is 3 μm, and the outer radius of the ring-structure region is 8.25 μm. The ACF is fabricated by the standard modified

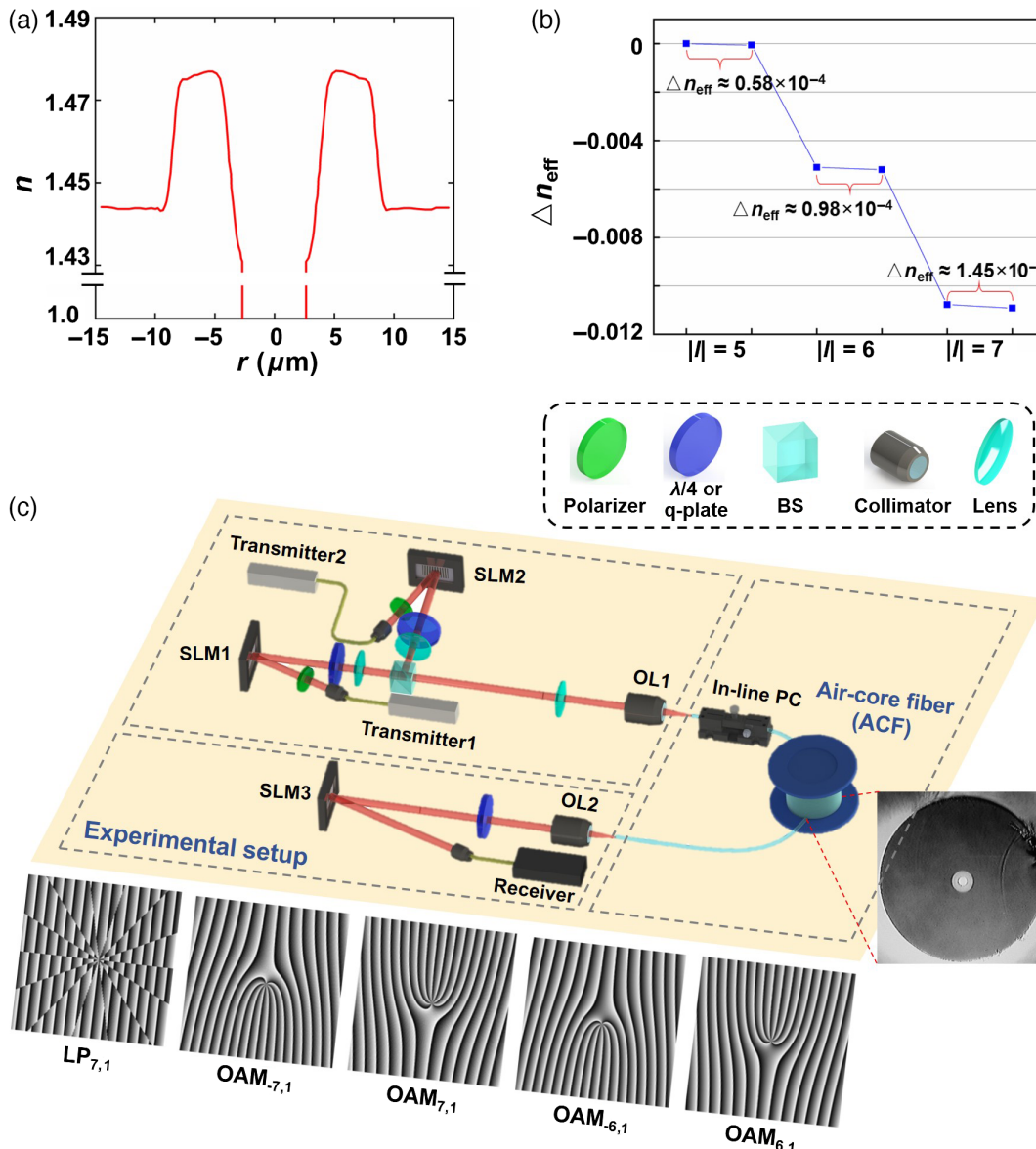


Fig. 2 Characterization of the ACF and experimental setup for spatial modes transmission in ACF. (a) Measured refractive index profile of the ACF. (b) The Δn_{eff} between adjacent OAM modes within each OAM mode group for $|l| = 5, 6, 7$ in the ACF. (c) Experimental setup for spatial modes (LP, LP-OAM, vector, and CP-OAM) transmission in ACF. Right inset, optical microscope image of the ACF facet. Bottom insets, phase patterns loaded onto SLM to generate $\text{LP}_{7,1}$, $\text{OAM}_{7,1}$, $\text{OAM}_{7,1}$, $\text{OAM}_{-6,1}$, and $\text{OAM}_{6,1}$ modes. SLM, spatial light modulator; OL, objective lens; BS, beam splitter; PC, polarization controller.

chemical vapor deposition method. The ring-structure design benefits the suppression of high-order radial modes. The high-index contrast between the ring-structure and cladding helps to lift the mode degeneracy of OAM modes, including high-order HE and EH modes, $\text{OAM}_{l,m}^{\sigma+}/\text{OAM}_{-l,m}^{\sigma-}$ and $\text{OAM}_{l,m}^{\sigma-}/\text{OAM}_{-l,m}^{\sigma+}$ modes with the same $|l|$, and OAM modes with different $|l|$. The Δn_{eff} between adjacent OAM modes within each OAM mode group for $|l| = 5, 6, 7$ is depicted in Fig. 2(b). It should be noted that OAM modes with different $|l|$ (i.e., different OAM mode groups) have large Δn_{eff} ($> 1 \times 10^{-3}$). Particularly, in each mode group, HE and EH modes, or $\text{OAM}_{l,m}^{\sigma+}/\text{OAM}_{-l,m}^{\sigma-}$

and $\text{OAM}_{l,m}^{\sigma-}/\text{OAM}_{-l,m}^{\sigma+}$ modes with the same $|l|$, also have a relatively large Δn_{eff} ($> 0.5 \times 10^{-4}$), which increases with $|l|$ and helps to suppress the mode coupling. Such a distinct feature, which is not available in conventional weakly guiding fibers, is gained by the high-contrast-index ring-structure design of the ACF. The basic experimental setup is shown in Fig. 2(c). Spatial light modulators (SLMs) are used to generate LP modes or LP-OAM modes by properly switching the loaded phase patterns. Several typical examples of phase patterns loaded onto the SLMs are depicted in the insets of Fig. 2(c). The polarizers are aligned to the working direction of SLMs, and the proper

adjustment of polarization states in the transmitters [not shown in Fig. 2(c)] optimizes the power. To generate CP-OAM modes, quarter-wave plates (QWPs) are added to convert the linear polarization to circular polarization (i.e., LP-OAM to CP-OAM). To generate vector modes, the QWP is replaced with a q-plate. Since the q-plate can convert CP Gaussian mode to CP OAM mode with reversed SAM, it can also produce vector modes with linear polarization inputs. This is because the vector modes can be regarded as the linear combination of CP-OAM modes, and the LP input can be decomposed into the left-handed CP (LCP) and right-handed CP (RCP) components. In this case, the phase patterns loaded onto SLMs are changed to gratings, and SLMs function as mirrors. At the receiver side, another SLM loaded with specific phase patterns is used to detect the LP and OAM modes, i.e., converting back to Gaussian-like beams and coupling to fibers for detection. To detect LP and LP-OAM modes, the QWP is replaced with a half-wave plate (HWP) to optimize the polarization direction. To detect CP-OAM modes, the QWP converts the linear polarization back from the circular polarization (i.e., CP-OAM to LP-OAM). To detect vector modes, the QWP is replaced with a q-plate. To characterize the basic properties of different mode bases, only a single channel is used at the transmitter side in the experimental setup. To carry out the system-level experiments of MDM fiber-optic communications, two channels are used at the transmitter side for proof-of-concept demonstration, where a beam splitter (BS) is simply used to combine the two data channels and is coupled into the fabricated 1-km ACF via an objective lens (OL). An in-line PC is put on the ACF to induce one kind of fiber perturbation. Other kinds of fiber perturbations are exerted by pressing the fiber, winding the fiber into small circles, and lifting the fiber out of plane. The measured fiber facet microscope image of the fabricated ACF is shown in the inset of Fig. 2(c). After single-channel transmission or two-channel MDM transmission through the 1-km ACF, LP modes (by SLM), LP-OAM modes (by SLM), CP-OAM modes (by QWP and SLM), and vector modes (by q-plate) are converted back to Gaussian-like modes for detection. For system-level single-channel transmission or MIMO-free two-channel MDM transmission experiments, only one set of detection at the receiver side is required (one after another detection for MIMO-free MDM). For two-channel MDM transmission with significant mode coupling and cross talk, two sets of detection are required to simultaneously receive two-channel signals with mutual cross talk.

3.1 Characterization of Different Spatial Mode Bases

First, we characterize basic properties of different spatial mode bases when they propagate through the ACF. Figures 3(a)–3(d) show measured typical intensity profiles of LP, LP-OAM, CP-OAM, and vector modes, respectively. The LP modes feature petal-like patterns. The LP-OAM, CP-OAM, and vector modes show doughnut-shaped intensity profiles due to phase and polarization singularities at the beam center. We measure the stability of different spatial mode bases (LP, LP-OAM, CP-OAM, and vector modes) in ACF (see Figs. 4–8). The LP and LP-OAM modes are not stable and easy to convert to each other after fiber propagation (see Figs. 4 and 5). Figures 3(a) and 3(b) show captured images in an instant. To verify the CP-OAM modes, we use a polarization beam displacer (PBD) after the QWP at the receiver side to detect the circular polarization [not

shown in Fig. 2(c)]. Meanwhile, the OAM orders are measured by the interference with an expanded reference Gaussian beam, as shown in Fig. 3(c). The number of twists and the twisting direction determine the magnitude and sign of OAM orders. The CP-OAM modes, including the degenerate CP-OAM modes within a mode group, are stable under fiber perturbations as analyzed above (see Figs. 7 and 8). To verify the vector modes, we use a rotating polarizer [not shown in Fig. 2(c)] and the observed petal-like patterns after the polarizer confirm the generation of vector modes, as shown in Fig. 3(d). The vector modes can be converted back to Gaussian-like beams by the q-plate. The degenerate even and odd vector modes are not stable under out-of-plane fiber movement perturbations (see Fig. 6).

We investigate the walk-off effect of different spatial mode bases by employing a pulsed laser source. The period of the pulsed laser is 12.5 ns, which is larger than the DGD among different modes after passing through the 1-km ACF. This ensures that the walk-off pulse and the periodically repeating pulse are easily distinguished. Figures 3(e)–3(j) show measured temporal waveforms by an oscilloscope (pulse response) after 1-km ACF transmission when launching LP, LP-OAM, vector, and CP-OAM modes to the ACF. ACF transmissions without and with perturbations are measured. Figures 3(e) and 3(f) show measured results for LP_{7,1} and LP-OAM_{7,1} modes, respectively, without fiber perturbations. One can clearly see two splitting pulses, showing the walk-off effect of LP and LP-OAM modes even without fiber perturbations. These are because both LP and LP-OAM modes are composed of non-degenerate HE and EH modes with different propagation constants. The two splitting pulses have a measured time interval of about 1.13 ns (EH_{6,1} and HE_{8,1}) in Figs. 3(e) and 3(f), which are in good agreement with the theory (DGD between EH_{6,1} and HE_{8,1}: ~1.134 ns/km). Figures 3(g) and 3(h) show measured results for EH_{6,1} and CP-OAM_{7,1} modes, respectively, without fiber perturbations. Only one single pulse is observed after 1-km ACF transmission, showing no walk-off effect. Particularly, even under fiber perturbations (e.g., out-of-plane fiber movement), one can still only observe one single pulse after 1-km ACF transmission for EH_{6,1} and CP-OAM_{7,1} modes, as shown in Figs. 3(i) and 3(j), respectively, which are consistent with the theory.

Despite no walk-off effect, the degenerate even and odd vector modes can easily couple with each other due to an extra geometric phase induced by out-of-plane fiber movements, which cannot be seen from the pulse response measurement in Fig. 3(i). In the experiment, for the vector mode basis, we employ a PBD after the q-plate to split and simultaneously detect the power of even and odd vector modes by a camera. As a result, we can measure the relative power of even and odd vector modes under out-of-plane fiber movements. As shown in Fig. 3(k) (launching mode: EH_{6,1}^{even}), significant power coupling between EH_{6,1}^{even} and EH_{6,1}^{odd} is observed, and complete mode coupling is possible. In contrast, for the CP-OAM mode basis, we also use a PBD after the QWP to split and simultaneously detect the relative power of degenerate CP-OAM modes by a camera under out-of-plane fiber movements. As shown in Fig. 3(l) (launching mode: OAM_{-7,1}^{σ+}), negligible power coupling between OAM_{-7,1}^{σ+} and OAM_{-7,1}^{σ-} modes is observed. The power of coupled OAM_{-7,1}^{σ+} mode remains <−15 dB compared to that of the launched OAM_{-7,1}^{σ+} mode. The measured results in Figs. 3(k) and 3(l) indicate that the degenerate vector modes are susceptible, while the degenerate high-order CP-OAM modes are stable against the out-of-plane fiber movement perturbations.

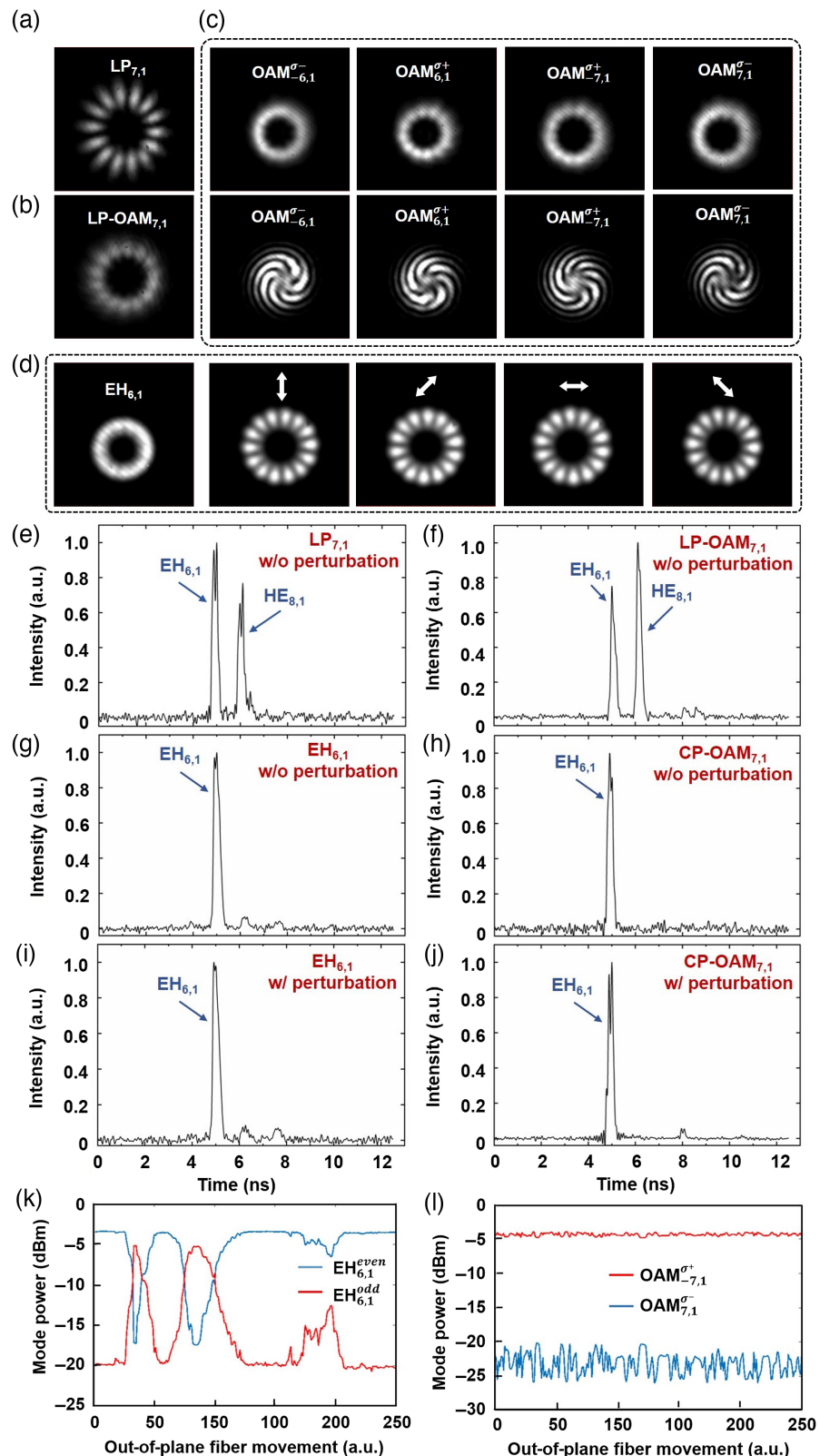


Fig. 3 Basic properties of spatial modes transmission in ACF. (a)–(d) Measured intensity profiles of different spatial modes after 1-km ACF transmission. (a) LP_{7,1} mode; (b) LP-OAM_{7,1} mode; (c) CP-OAM modes (top, doughnut-shaped intensity profiles; bottom, interference patterns with a reference Gaussian beam); (d) vector mode (EH_{6,1}) and its intensity profiles after passing through a rotating linear polarizer. (e)–(j) Pulse response of different spatial modes after 1-km ACF transmission. (e) LP_{7,1} without perturbation; (f) LP-OAM_{7,1} without perturbation;

Fig. 3 (Continued) (g) EH_{6,1} without perturbation; (h) CP-OAM_{7,1} without perturbation; (i) EH_{6,1} with perturbation; (j) CP-OAM_{7,1} with perturbation. w/: with. w/o: without. (k), (l) Power evolution of degenerate vector modes and degenerate CP-OAM modes under out-of-plane fiber movements. (k) Launching mode: EH_{6,1}^{even}; (l) launching mode: OAM_{-7,1}⁺.

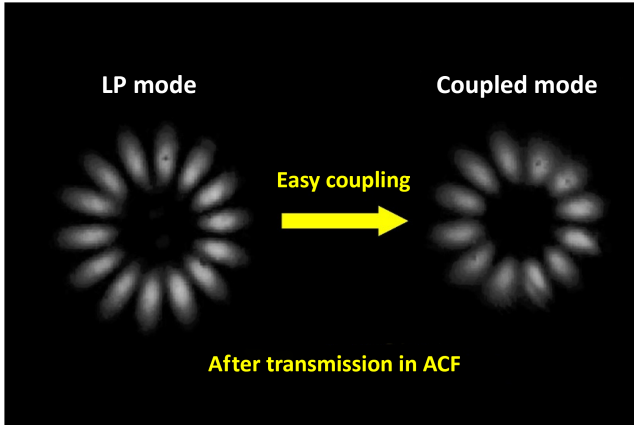


Fig. 4 Measured intensity profiles of LP mode and its coupled mode after transmission in ACF. Easy coupling is observed ([Video 1, MP4, 2.55 MB \[URL: <https://doi.org/10.1117/1.AP.5.5.056003.s1>\]](https://doi.org/10.1117/1.AP.5.5.056003.s1)).

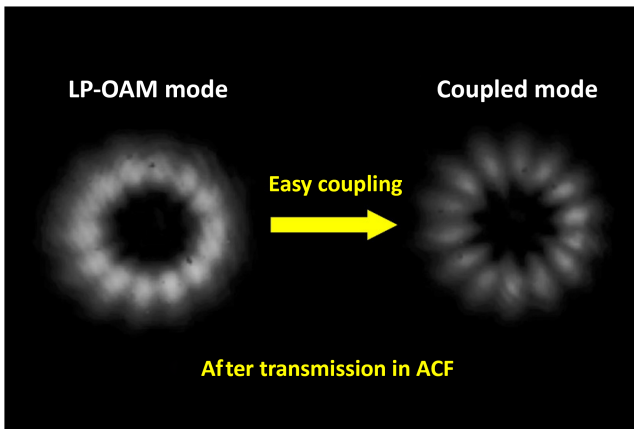


Fig. 5 Measured intensity profiles of LP-OAM mode and its coupled mode after transmission in ACF. Easy coupling is observed ([Video 2, MP4, 2.33 MB \[URL: <https://doi.org/10.1117/1.AP.5.5.056003.s2>\]](https://doi.org/10.1117/1.AP.5.5.056003.s2)).

3.2 Single-Channel Transmission with Different Spatial Modes

Second, we comprehensively evaluate the system-level BER performance for data-carrying single-channel transmission over the 1-km ACF with different spatial modes. For the single-channel system-level demonstration, the details of the transmitter and receiver in Fig. 2(c) are shown in Fig. 9(a). At the transmitter, a continuous-wave laser at 1550 nm is modulated by an in-phase/quadrature (I/Q) modulator driven by an arbitrary waveform generator (AWG) to generate a 12.5-Gbaud 8-ary quadrature amplitude modulation (8-QAM) signal. An erbium-doped fiber amplifier (EDFA) and a PC are used to boost the power and

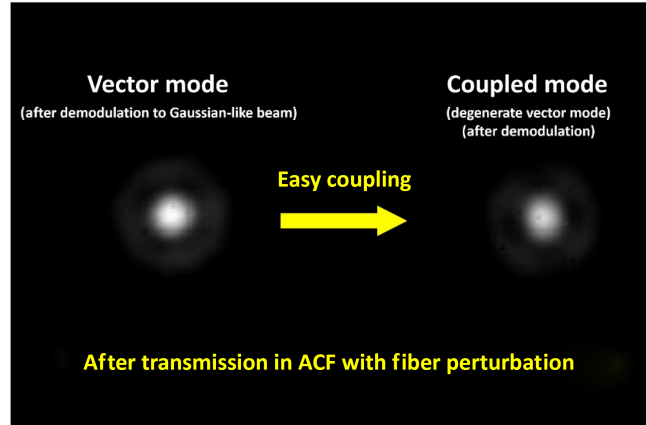


Fig. 6 Measured intensity profiles of vector mode and its coupled degenerate vector mode (after demodulation by a q-plate to Gaussian-like beam with bright spot at the beam center) after transmission in ACF under out-of-plane fiber movement perturbation. Easy coupling is observed ([Video 3, MP4, 1.40 MB \[URL: <https://doi.org/10.1117/1.AP.5.5.056003.s3>\]](https://doi.org/10.1117/1.AP.5.5.056003.s3)).

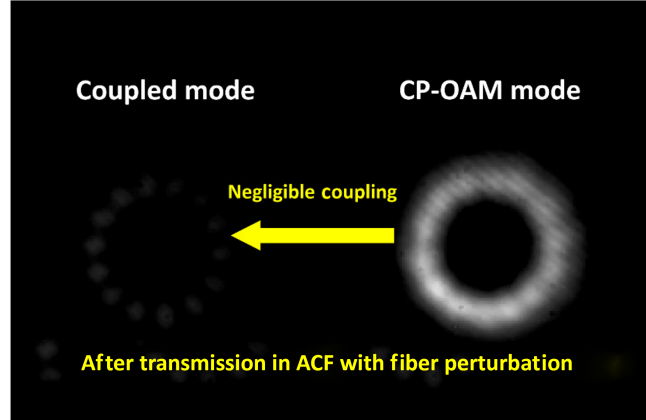


Fig. 7 Measured intensity profiles of CP-OAM mode and its coupled degenerate CP-OAM mode after transmission in ACF under out-of-plane fiber movement perturbation. Negligible coupling is observed ([Video 4, MP4, 1.51 MB \[URL: <https://doi.org/10.1117/1.AP.5.5.056003.s4>\]](https://doi.org/10.1117/1.AP.5.5.056003.s4)).

adjust the polarization state of the optical signal. At the receiver, the optical signal is amplified by an EDFA. A variable optical attenuator (VOA) followed by another EDFA is used to adjust the received optical signal-to-noise ratio (OSNR) for BER measurement. Another laser serves as the local oscillator (LO) to mix with the received optical signal by an optical hybrid, the outputs of which are sent to an oscilloscope followed by the offline DSP. Figure 9(b) plots the measured BER curves for data-carrying single-channel transmission over the 1-km ACF with LP mode, LP-OAM mode, vector mode, and CP-OAM

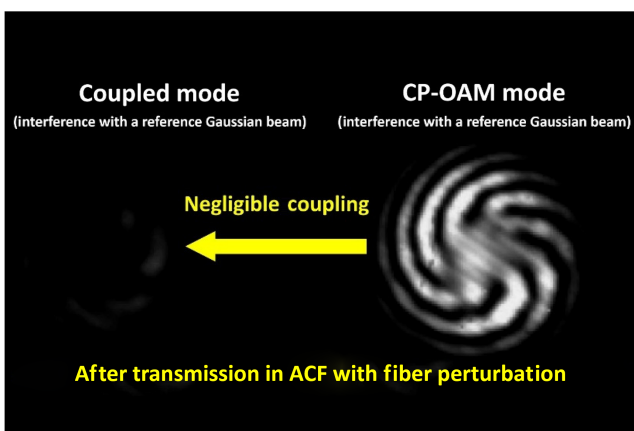


Fig. 8 Measured intensity profiles of CP-OAM mode (interference with a reference Gaussian beam) and its coupled degenerate CP-OAM mode (interference with a reference Gaussian beam) after transmission in ACF under out-of-plane fiber movement perturbation. Negligible coupling is observed ([Video 5, MP4, 3.15 MB \[URL: <https://doi.org/10.1117/1.AP.5.5.056003.s5>\]](https://doi.org/10.1117/1.AP.5.5.056003.s5)).

mode. Two sets of BER curves are measured, i.e., one without fiber perturbations (solid markers) and the other with fiber perturbations (hollow markers) by adjusting the in-line PC on the ACF. For LP and LP-OAM modes, the measured BER values are always far above the soft-decision forward-error correction (SD-FEC) threshold of 1.5×10^{-2} , whether or not fiber perturbations are induced. These are due to the intrinsic walk-off effect of LP and LP-OAM modes and accompanied mode coupling. For vector modes, the measured BER values show excellent performance without fiber perturbations. Some performance degradation, with an OSNR penalty of ~ 3.5 dB compared to the case without fiber perturbations, is observed for vector modes under fiber perturbations by adjusting the in-line PC. This might be ascribed to the power coupling of vector modes under fiber perturbations. However, the BER values can be still below the hard-decision forward-error correction (HD-FEC) threshold of 3.8×10^{-3} . For CP-OAM modes, one can clearly see very similar BER performance for 1-km ACF transmission without and with fiber perturbations. The measured OSNR penalties are only about 1 dB compared to the back-to-back case at a BER of 1.5×10^{-2} (SD-FEC threshold). Figure 9(c) shows measured typical constellations for LP mode, LP-OAM mode, vector mode, and CP-OAM mode after 1-km ACF transmission as well as the back-to-back case.

To further show the impact of different kinds of fiber perturbations on data-carrying single-channel transmission over the 1-km ACF, we also measure the BER performance with each kind of varied fiber perturbation (i.e., dynamic BER performance under each kind of fiber perturbation). Four typical kinds of fiber perturbations are taken into consideration in the experiment, i.e., adjusting the in-line PC (pressing, twisting, and slight out-of-plane fiber movement), significant out-of-plane fiber movement, putting weight on the fiber to add pressure (pressing) (maximum weight: 1.62 kg), and winding the fiber into small circles (bending, slight twisting, and slight out-of-plane fiber movement) (0 to 4 circles, 12.7-mm diameter for each circle). The initial value of OSNR is set to 16 dB. The measured results for LP_{7,1} mode, LP-OAM_{7,1} mode, EH_{6,1} vector mode, and CP-OAM_{7,1} mode under different kinds of fiber perturbations are

shown in Figs. 9(d)–9(g), respectively. One can see the measured BER values for LP and LP-OAM modes are always above the HD-FEC threshold (3.8×10^{-3}) even for the single-channel transmission, showing severely degraded performance. For vector modes, as shown in Fig. 9(f), the BER performance remains almost unchanged under the pressure perturbation (in-plane perturbation). However, the BER performance for vector modes suffers some degradation under other kinds of fiber perturbations, such as adjusting the in-line PC, significant out-of-plane movement, and winding the fiber into small circles, as shown in Figs. 9(d), 9(e), and 9(g). Under the varied fiber perturbations, the BER values can be above the HD-FEC threshold (3.8×10^{-3}). These could be explained with the fact that fiber perturbations with out-of-plane movements cause the power coupling of vector modes. Remarkably, as shown in Figs. 9(d)–9(g), the BER performance for CP-OAM modes stays almost unchanged and always below the HD-FEC threshold (3.8×10^{-3}) under all kinds of varied fiber perturbations.

The measured system-level results for data-carrying single-channel transmission indicate that the CP-OAM mode basis shows impressive performance against various kinds of fiber perturbations. This implies the great potential for using the CP-OAM mode basis in MDM fiber-optic communications.

3.3 Two-Channel MDM Transmission Using Vector Modes and CP-OAM Modes

Third, we comprehensively assess the system-level BER performance for data-carrying two-channel MDM transmission over the 1-km ACF using vector modes and CP-OAM modes. Since LP and LP-OAM modes show significantly worse BER performance compared to vector and CP-OAM modes in data-carrying single-channel transmission systems, for the following MDM transmission system, we only focus on the comparison between vector and CP-OAM modes and choose two-channel MDM transmission for simple proof-of-concept demonstration. For the two-channel MDM system-level demonstration, the details of the transmitter, receiver, and MDM configuration are shown in Figs. 10(a)–10(d). At the transmitter, as shown in Fig. 10(a), a 10-Gbaud quadrature phase-shift keying (QPSK) signal or a 12.5-Gbaud 8-QAM signal is prepared, which is divided into two paths with one path delayed by a 1-km SMF compared to the other for decorrelation. As a result, two-channel signals are generated, with their power boosted by EDFA. At the receiver, for the MIMO-free MDM transmission with negligible mode coupling (e.g., CP-OAM modes), only one set of detection is required, as depicted in Fig. 2(c). For the MIMO-DSP enabled MDM transmission with significant mode coupling (e.g., degenerate vector modes), two sets of detection are required, as depicted in Fig. 10(b). Two-channel received signals with mode coupling after 1-km ACF transmission are mixed with the LO (10-GHz frequency offset compared to the signal) and detected by two photodetectors (PDs) based on the heterodyne coherent detection scheme. The received two-channel electrical signals after analog-to-digital conversion (ADC) are used for 2×2 MIMO-DSP to mitigate the mode cross talk for BER performance measurement. Due to available lab conditions with a limited number of q-plates, we employ another two sets of loop structure to generate two-channel vector modes at the transmitter in the MDM transmission experiment, as shown in Fig. 10(d). At the receiver, two q-plates are used to convert the two-channel vector modes back to Gaussian-

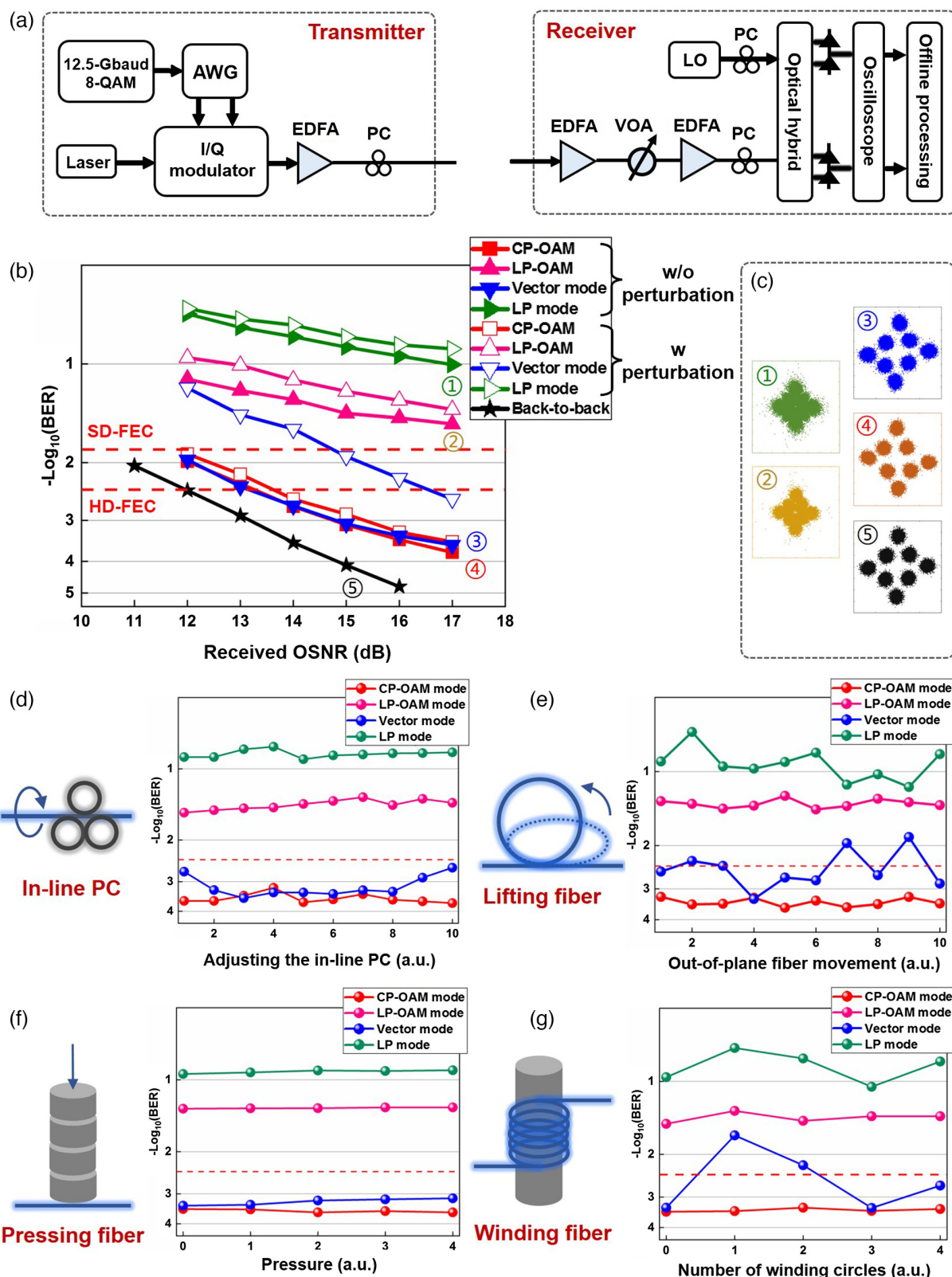


Fig. 9 Transmitter, receiver, and system-level performance for data-carrying single-channel transmission in ACF with different spatial modes. (a) Experimental configuration of the transmitter and receiver. AWG, arbitrary waveform generator; 8-QAM, 8-ary quadrature amplitude modulation; I/Q modulator, in-phase/quadrature modulator; EDFA, erbium-doped fiber amplifier; PC, polarization controller; VOA, variable optical attenuator; LO, local oscillator. (b) Measured BER curves for LP, LP-OAM, vector, and CP-OAM modes without and with fiber perturbations.

Fig. 9 (Continued) OSNR, optical signal-to-noise ratio; HD-FEC, hard-decision forward-error correction ($\text{BER} = 3.8 \times 10^{-3}$); SD-FEC, soft-decision forward-error correction ($\text{BER} = 1.5 \times 10^{-2}$). (c) Constellations of 8-QAM signals in (b). (d)–(g) Measured dynamic BER performance under each kind of varied fiber perturbation. (d) Adjusting the in-line PC; (e) out-of-plane fiber movement; (f) putting weight on the fiber to add pressure; (g) winding the fiber into small circles.

like beams, which are coupled to SMFs for detection. The loop structure incorporating a vortex phase plate (VPP) for the generation of vector modes is illustrated in Fig. 10(c). The operation principle still relies on the linear combination of two CP-OAM modes for the generation of vector modes. The incident LP Gaussian beam is rotated to 45 deg linear polarization by an HWP. After passing through a polarization beam splitter (PBS), the Gaussian beam is divided into x - and y -polarization components, propagating along clockwise and counterclockwise directions, respectively. A polarization-independent VPP incorporated into the loop structure adds a spiral phase front to the Gaussian beam and converts it to the OAM beam. Note that the VPP generates two LP-OAM modes with inverted sign for clockwise and counterclockwise propagation beams. The x - and y -polarization OAM modes are combined again by the PBS followed by a QWP. Both x - and y -polarization OAM modes experience twice the reflections by the mirror or PBS, so the sign of their OAM orders remains inverted. The QWP further converts the x - and y -polarization OAM modes with inverted sign to two CP-OAM modes with inverted OAM charge, respectively. As a result, the vector mode synthesized by two CP-OAM modes is generated. Particularly, different kinds of vector modes, including the degenerate even and odd ones ($\text{HE}_{l+1,m}^{\text{even}}$ and $\text{HE}_{l+1,m}^{\text{odd}}$ or $\text{EH}_{l-1,m}^{\text{even}}$ and $\text{EH}_{l-1,m}^{\text{odd}}$), can be generated by properly adjusting the axis of the QWP. It is worth noting that the proposed loop structure scheme for the generation of vector modes in Fig. 10(c) has the distinct advantages of high quality and high stability. This is because the clockwise and counterclockwise propagation beams in the loop structure share the same path, and the generation scheme is stable and robust against environmental disturbance.

Figure 10(e) plots the measured BER curves for data-carrying (10-Gbaud QPSK signal) two-channel MDM transmission over the 1-km ACF using degenerate even and odd vector modes (e.g., $\text{EH}_{6,1}^{\text{even}}$ and $\text{EH}_{6,1}^{\text{odd}}$ modes) under out-of-plane fiber movement perturbations. The mode cross talk is inevitable due to the geometric phase caused by out-of-plane fiber movement perturbations. The amount of mode cross talk is controllable by properly changing the degree of fiber perturbations. In the experiment, we adjust the degree of lifting the fiber out of plane to introduce two sets of mode cross talk value, i.e., one with -4 dB moderate cross talk and the other with 0 dB severe cross talk. For the moderate cross talk, the BER values of two channels are above the HD-FEC threshold (3.8×10^{-3}). Hence, MIMO-DSP is especially required to mitigate the cross talk to be used in MDM fiber-optic communications at the price of increased complexity and DSP-induced power consumption. In particular, for the severe cross talk, the BER performance after MDM transmission gets even worse. The mode cross talk cannot be mitigated even if the MIMO-DSP is applied. These set great limitations on MDM transmission using degenerate even and odd vector modes under fiber perturbations.

Figure 10(f) plots the measured BER curves for data-carrying (12.5-Gbaud 8-QAM signal) two-channel MDM transmission

over the 1-km ACF using degenerate CP-OAM modes (e.g., $\text{OAM}_{7,1}^{\sigma^-}$ and $\text{OAM}_{7,1}^{\sigma^+}$) under out-of-plane fiber movement perturbations. Remarkably, MIMO-free MDM transmission is achieved due to the intrinsic high stability of degenerate CP-OAM modes (low-level cross talk of about -17 dB), leading to superior performance with only <1.5 -dB OSNR penalty compared to the back-to-back case at a BER of 3.8×10^{-3} (HD-FEC threshold). The insets of Fig. 10(f) show typical constellations of 8-QAM signals.

For data-carrying MDM transmission with degenerate $\text{OAM}_{7,1}^{\sigma^-}$ and $\text{OAM}_{7,1}^{\sigma^+}$ modes, we also measure the dynamic BER performance under each kind of varied fiber perturbation. The initial value of OSNR is set to 16 dB. Figure 10(g) depicts the dynamic BER performance by adjusting the in-line PC and under out-of-plane fiber movement. Figure 10(h) displays the dynamic BER performance by putting weight on the fiber to add pressure. Figure 10(i) shows the dynamic BER performance by winding the fiber into small circles. For all kinds of fiber perturbations, the measured results show impressive BER performance for MDM transmission using degenerate $\text{OAM}_{7,1}^{\sigma^-}$ and $\text{OAM}_{7,1}^{\sigma^+}$ modes without the need of MIM-DSP.

In addition to degenerate $\text{OAM}_{7,1}^{\sigma^-}$ and $\text{OAM}_{7,1}^{\sigma^+}$ modes with the SAM and OAM anti-aligned (i.e., linear combination of $\text{EH}_{6,1}^{\text{even}}$ and $\text{EH}_{6,1}^{\text{odd}}$ modes), we also consider the data-carrying (12.5-Gbaud 8-QAM signal) two-channel MDM transmission over the 1-km ACF using another kind of degenerate CP-OAM modes, i.e., degenerate $\text{OAM}_{6,1}^{\sigma^+}$ and $\text{OAM}_{-6,1}^{\sigma^-}$ modes with the SAM and OAM aligned (linear combination of $\text{HE}_{7,1}^{\text{even}}$ and $\text{HE}_{7,1}^{\text{odd}}$ modes). The measured BER curves and typical constellations under out-of-plane fiber movement are shown in Fig. 11(a). For other kinds of fiber perturbations, such as adjusting the in-line PC, the measured dynamic BER performance is depicted in Fig. 11(b). Favorable operation performance is achieved using degenerate $\text{OAM}_{6,1}^{\sigma^+}$ and $\text{OAM}_{-6,1}^{\sigma^-}$ modes for MIMO-free MDM transmission.

The two-channel OAM modes in Figs. 10(f)–10(i) or Figs. 11(a) and 11(b) are within the same mode group. Additionally, we also study the data-carrying (12.5-Gbaud 8-QAM signal) two-channel MDM transmission over the 1-km ACF using two CP-OAM modes from different mode groups (e.g., $\text{OAM}_{-6,1}^{\sigma^-}$ and $\text{OAM}_{-7,1}^{\sigma^+}$ modes). Figure 11(c) plots the measured BER curves and typical constellations under out-of-plane fiber movement. Less than 1-dB OSNR penalty compared to the back-to-back case at a BER of 3.8×10^{-3} (HD-FEC threshold) is achieved for MIMO-free MDM transmission with $\text{OAM}_{-6,1}^{\sigma^-}$ and $\text{OAM}_{-7,1}^{\sigma^+}$ modes. Figures 11(d)–11(g) depict the dynamic BER performance under each kind of varied fiber perturbation (initial value of OSNR: 16 dB), i.e., adjusting the in-line PC [Fig. 11(d)], under out-of-plane fiber movement [Fig. 11(e)], putting weight on the fiber to add pressure [Fig. 11(f)], and winding the fiber into small circles [Fig. 11(g)]. The measured results in Figs. 11(c)–11(g) indicate outstanding performance for MIMO-free MDM transmission using CP-OAM modes from different mode groups. This can

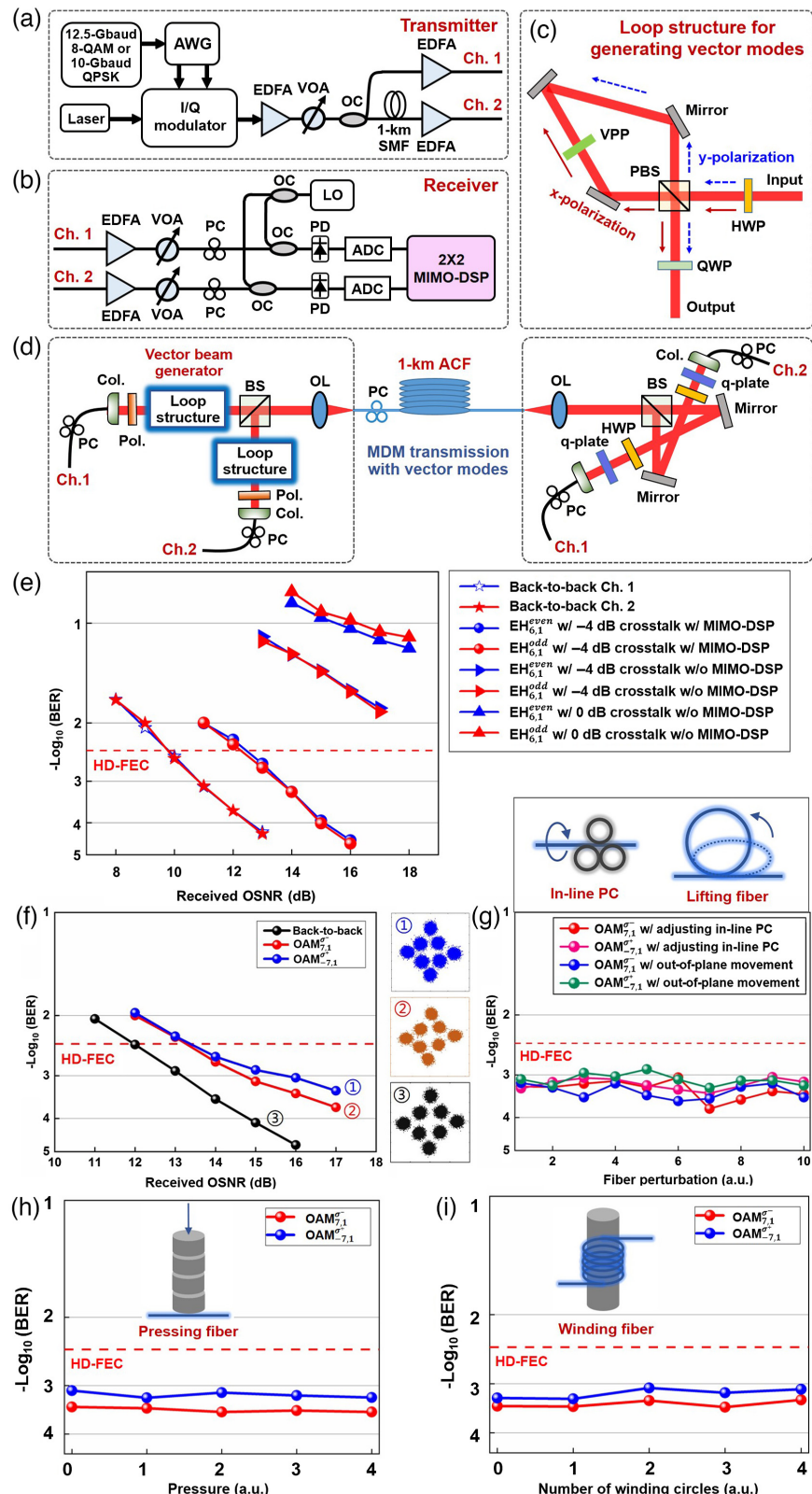


Fig. 10 Transmitter, receiver, loop structure, setup, and system-level performance for data-carrying two-channel MDM transmission in ACF with degenerate vector modes and degenerate CP-OAM modes (SAM and OAM anti-aligned). (a) Transmitter. AWG, arbitrary waveform generator; 8-QAM, 8-ary quadrature amplitude modulation; QPSK, quadrature phase-shift keying; I/Q modulator, in-phase/quadrature modulator; EDFA, erbium-doped fiber amplifier; VOA, variable optical attenuator; OC, optical coupler; SMF, single-mode fiber. (b) Receiver. PC, polarization controller;

Fig. 10 (Continued) LO, local oscillator; PD, photodetector; ADC, analog-to-digital converter; MIMO-DSP, multiple-input multiple-output digital signal processing. (c) Loop structure incorporating a VPP for the generation of vector modes. VPP, vortex phase plate; PBS, polarization beam splitter; QWP, quarter-wave plate. (d) Experimental configuration for two-channel MDM transmission in ACF with degenerate vector modes. LO, local oscillator. (e) Measured BER curves for MDM transmission in ACF with degenerate even and odd vector modes under out-of-plane fiber movement perturbation. (f) Measured BER curves for MIMO-free MDM transmission in ACF with degenerate CP-OAM modes under out-of-plane fiber movement perturbation. Insets, constellations of 8-QAM signals. (g)–(i) Measured dynamic BER performance under each kind of varied fiber perturbation. (g) Adjusting the in-line PC and out-of-plane fiber movement; (h) putting weight on the fiber to add pressure; (i) winding the fiber into small circles.

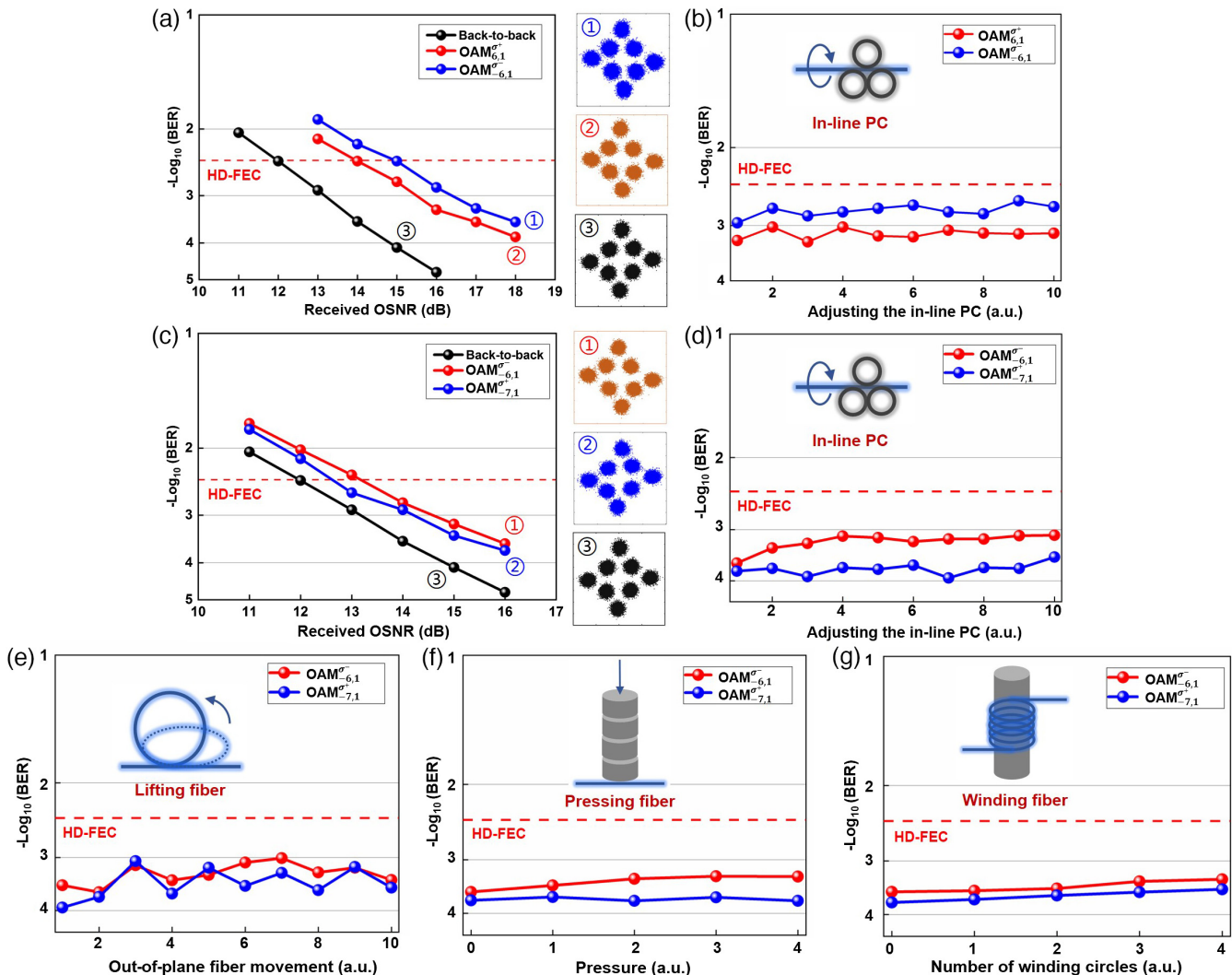


Fig. 11 System-level performance for data-carrying two-channel MDM transmission in ACF with degenerate CP-OAM modes (SAM and OAM aligned) from the same mode group or CP-OAM modes from different mode groups. (a), (b) Degenerate CP-OAM modes (SAM and OAM aligned) from the same mode group. (a) Measured BER curves for MIMO-free MDM transmission in ACF with degenerate CP-OAM modes under out-of-plane fiber movement perturbation. Insets, constellations of 8-QAM signals. (b) Measured dynamic BER performance when adjusting the in-line PC. (c)–(g) CP-OAM modes from different mode groups. (c) Measured BER curves for MIMO-free MDM transmission in ACF with CP-OAM modes under fiber perturbation. (d)–(g) Measured dynamic BER performance under each kind of varied fiber perturbation. (d) Adjusting the inline PC and out-of-plane fiber movement; (e) out-of-plane fiber movement; (f) putting weight on the fiber to add pressure; (g) winding the fiber into small circles.

be briefly explained as follows. On one hand, CP-OAM modes from different mode groups are not degenerate with large Δn_{eff} , which is beneficial to suppress the mode cross talk; on the other hand, the CP-OAM mode in each mode group is also stable itself without power loss (i.e., power coupling to other degenerate CP-OAM mode within the same mode group).

The experimental results in Figs. 3 and 9–11 are for 1-km ACF based on the existing laboratory conditions, and CP-OAM modes show high stability and robustness against various fiber perturbations. It is expected the transmission stability might also be maintained for longer ACF (e.g., 10-km ACF) considering the following aspects.

The perturbations (bending, twisting, pressing, winding, and moving) applied to the fiber in the experiment are significant. That is, the impact of applied fiber perturbations on the communication performance is greater than the impact of fiber imperfections. Hence, for longer ACF, especially with future improved fiber fabrication technique and optimized fiber performance, one would still expect high transmission stability and robustness against fiber perturbations.

According to the theoretical analyses from Eqs. (6)–(9), for the ACF used in the experiment, the high-contrast-index design with ACF structure facilitates significant mode separation both for CP-OAM modes from different mode groups ($\Delta n_{\text{eff}} > 1 \times 10^{-3}$) and for high-order nondegenerate CP-OAM modes in each mode group, which are beneficial to maintain the transmission stability for longer ACF. Due to the angular momentum conservation condition, which is not easily satisfied, the mode coupling between degenerate CP-OAM modes within the same mode group is also negligible, especially for large $|l|$. Moreover, based on the theoretical analyses from Eqs. (10)–(12), the local out-of-plane fiber movement perturbation (i.e., moving or lifting the fiber out of the plane) only introduces an extra geometric phase to the CP-OAM modes themselves but does not cause mode coupling between degenerate CP-OAM modes within the same mode group, which is also independent of fiber length. Thus the transmission stability is expected to be maintained for 10 km or an even longer ACF.

In practical applications with possible unpredictable or more complex fiber perturbations, even if the transmission stability for a 10 km or longer ACF might be degraded slightly, the superiority of CP-OAM modes could still be expected when compared to other mode bases (LP modes, vector modes, and LP-OAM modes). Meanwhile, in the present 1-km fiber transmission experiment, 8-QAM signals are employed in Figs. 10(f)–10(i) and Figs. 11(a)–11(g). For other modulation format signals, such as QPSK with large cross talk tolerance, one would expect the feasibility of MDM transmission over 10 km or an even longer ACF with favorable system performance.

In the experiment, we demonstrate the transmission stability for high-order CP-OAM modes, i.e., $|l| = 6, 7$, as shown in Figs. 10 and 11. One would also expect the relatively good transmission stability for relatively low-order CP-OAM modes in the ACF, especially for CP-OAM modes from different mode groups. Remarkably, even if low-order CP-OAM modes in ACF have moderate transmission stability, the mode coupling may increase with the decrease of $|l|$, especially for the lowest-order modes (e.g., $|l| = 0, 1$). One may also use modulation format signals with relatively large cross talk tolerance (e.g., QPSK). Meanwhile, small-scale simplified MIMO-DSP might be used to mitigate the mode cross talk between the lowest-order modes.

With future improvement, flexible “mode engineering” (e.g., separation of the lowest-order modes) is expected to optimize the fiber structure to enhance the transmission stability of low-order modes, even for the lowest-order modes in fiber.

4 Discussions

4.1 Toward Practical Fiber Deployment with Complex Perturbations

In this work, we aim to find the superior mode basis for SDM/MDM fiber-optic communications in ACF. We give both theoretical analyses and system-level comparison in the experiment. We choose several representative fiber perturbations (bending, twisting, pressing, winding, and moving) in the proof-of-concept experiment, such as adjusting in-line PC (pressing, twisting, and slight out-of-plane fiber movement), significant out-of-plane fiber movement, putting weight on the fiber to add pressure (pressing), and winding the fiber into small circles (bending, slight twisting, and slight out-of-plane fiber movement). The obtained results show the superiority of the CP-OAM mode basis. Remarkably, in practical fiber deployment (cabling, installation, etc.) and realistic applications, more complex fiber perturbations would be encountered. From this point of view, more in-depth system-level studies are expected to further show the robustness of the CP-OAM mode basis in real application scenarios, such as data centers and high-performance computing with cabled ACF, especially under extreme working conditions.

4.2 Improved Fiber Design and Optimized Fiber Fabrication

The ACF employed in the experiment supports higher-order OAM modes and MIMO-free MDM transmission using degenerate CP-OAM modes up to the seventh order is demonstrated. From the above analyses, the mode stability of CP-OAM modes increases with the mode order $|l|$ based on the laws of angular momentum conservation. Improved fiber design (e.g., geometric parameters and refractive index profiles) supporting even higher-order OAM modes ($|l| > 10$) is expected so that more spatial modes with higher mode stability can be used to more effectively scale the transmission capacity and enhance the robustness against various fiber perturbations. The fabricated ACF has relatively large propagation loss ($\sim 1.9 \text{ dB/km}$ for $|l| = 5$ and $\sim 2.2 \text{ dB/km}$ for $|l| = 6$), mainly due to the high-contrast-index structure and fabrication imperfections. Future optimized fiber fabrication is expected to reduce the loss, considering the fact that some commercially available fibers, such as dispersion-compensating fibers also with high-contrast-index, show low-level loss around 0.5 dB/km . This will benefit long-distance MDM fiber-optic communications using the optimized ACF.

4.3 Efficient and Scalable Mode (De)multiplexers

To facilitate MDM transmission with a large number of OAM modes, an efficient and scalable mode (de)multiplexer is a key device that functions similarly to the wavelength (de)multiplexers in wavelength-division multiplexing transmission systems. Fortunately, there have been many works on scalable OAM (de)multiplexers, such as OAM mode sorter based on the Cartesian to log-polar coordinate transformation,⁴⁹ combination

of log-polar coordinate mapping and refractive beam copying,^{50,51} spiral transformation,⁵² and multi-plane light conversion.^{53,54} These OAM mode (de)multiplexers can efficiently separate multiple OAM modes with different l . However, additional discrete optical elements (e.g., lenses) are also required in the (de)multiplexing architecture. For MDM transmission in ACF with CP-OAM modes, a compact OAM mode (de)multiplexer is highly expected, with its input and output ports directly connected to the ACF and SMF array. Moreover, in order to take full use of all spatial modes, including OAM modes with the same l in each mode group, e.g., $OAM_{l,m}^{\sigma^-}$ and $OAM_{l,m}^{\sigma^+}$ or $OAM_{-l,m}^{\sigma^+}$ and $OAM_{-l,m}^{\sigma^-}$, OAM (de)multiplexers incorporating the SAM sorting function are desirable.

4.4 Superior Mode Basis in Diverse Fibers

There are many kinds of fibers widely used in SDM applications, such as FMF, MMF, RCF, ACF, multicore fiber (MCF), and multicore few-mode fiber. In this work, we mainly focus on the ACF and comprehensively study its superior mode basis for MDM transmission. We find the CP-OAM mode basis is the superior one in ACF for MDM transmission, especially for high-order CP-OAM modes. It is noted that the mode cross talk could be nonnegligible for low-order modes (e.g., $|l| = 0$ and 1) and proper DSP might be still required to mitigate the cross talk. One would expect “mode engineering” with optimized fiber structure to further separate the low-order modes (i.e., large Δn_{eff}). In addition to four kinds of spatial mode bases discussed in this work (i.e., LP modes, LP-OAM modes, vector modes, and CP-OAM modes), Eisenbud–Wigner–Smith states as principal modes in fibers have also attracted great interest.^{55,56} Moreover, enhanced spin–orbit interaction of light in highly confining optical fibers has also shown its potential in MDM transmission.²⁵ For diverse fibers supporting multiple spatial modes, more theoretical and experimental works are expected to find the most suitable mode basis in a specific fiber. Additionally, more comprehensive evaluation criteria should be considered, such as capacity, distance, cross talk, BER performance, robustness, MIMO-free/MIMO-DSP, complexity, and power consumption.

4.5 Superior Mode Basis in Complex Transmission Media

Beyond MDM transmission in fibers, versatile spatial modes (Laguerre–Gaussian beams, Hermite–Gaussian beams, vector beams, Bessel beams, Airy beams, Mathieu beams, pin-like beams, bottle beams, customized beams, arbitrarily structured light, etc.) have been also widely applied to data transmission through complex media (free-space, underwater, chip, etc.).⁵⁷ The spatial mode propagation in complex media is much more complicated compared to that in optical fibers. Diffraction, scattering, divergence, obstacle, turbulence, and other kinds of imperfections need to be considered. Different kinds of spatial modes also show their unique propagation properties, such as being diffraction-free, self-healing, non-line-of-sight, and turbulence-resilient.^{57,58} Very recently, turbulence-resilient pilot-assisted self-coherent free-space optical communications using automatic optoelectronic mixing of many modes,⁵⁹ compensation-free high-dimensional free-space optical communications using turbulence-resilient vector beams,⁶⁰ and robust vectorial structured light propagation in complex media⁶¹ have been proposed and demonstrated, showing impressive performance.

In the future, more and more works are expected to find the superior mode basis for data transmission in complex media.

4.6 Extended Applications of Versatile Spatial Modes in Fibers

Beyond SDM/MDM fiber-optic communications using spatial modes, more extended applications of versatile mode bases in fibers are expected, such as spin–orbit mapping,⁶² optical activity,⁶³ nonlinear optics,⁶⁴ optical metrology,⁶⁵ optical imaging,⁶⁶ and quantum science.^{67,68} For example, spin–orbit mapping of light in an FMF originating from the mode degeneracy lifting, high-resolution wave meter by enhanced optical activity in fibers, intermodal nonlinear mixing with Bessel beams in fibers, remote measurement of the angular velocity vector based on vectorial Doppler effect using ACF, time-of-flight 3D imaging through multimode optical fibers, and high-dimensional quantum cryptography with hybrid OAM states through RCF have been proposed and demonstrated, showing favorable performance. In the future, one would expect to see more emerging applications using versatile mode bases in different kinds of fibers. The newly added space degree of freedom of spatial modes in fibers provides more advanced applications beyond conventional SMF.

5 Conclusion

In summary, we have presented theoretical analyses and system-level experimental demonstrations on finding the superior spatial mode basis for MDM fiber-optic communications in ACF. The LP and LP-OAM modes have intrinsic mode walk-off effect, causing split pulse response and signal spreading as well as mode coupling. Despite no intrinsic mode walk-off effect, the degenerate even and odd vector modes ($HE_{l+1,m}^{\text{even}}$ and $HE_{l+1,m}^{\text{odd}}$ or $EH_{l-1,m}^{\text{even}}$ and $EH_{l-1,m}^{\text{odd}}$) can easily couple to each other due to extra geometric phase induced by out-of-plane fiber movements. In contrast, CP-OAM modes show high stability and robustness against various fiber perturbations, including high-order degenerate CP-OAM modes within the same mode group. Such superiority originates from the laws of angular momentum conservation. Particularly, we comprehensively compare the system-level BER performance for data-carrying single-channel and two-channel MDM transmission over the 1-km ACF with different spatial modes. Various kinds of fiber perturbations are considered, such as adjusting the in-line PC (pressing, twisting, and slight out-of-plane fiber movement), significant out-of-plane fiber movement, putting weight on the fiber to add pressure (pressing), and winding the fiber into small circles (bending, slight twisting, and slight out-of-plane fiber movement). The measured results indicate that LP and LP-OAM modes suffering mode walk-off and coupling are not suitable for data transmission in ACF; degenerate even and odd vector modes need MIMO-DSP with increased complexity to mitigate the moderate cross talk and may fail to recover the signal with severe cross talk for MDM transmission in ACF; high-order CP-OAM modes show impressive performance for MDM transmission in ACF under various kinds of fiber perturbations. The system-level demonstration shows that the CP-OAM mode basis is the superior one for MDM fiber-optic communications with ACF, which may find promising applications in short-reach MDM optical interconnects for data centers and high-performance computing. For the future, finding a superior mode basis in various kinds of fibers and other complex

transmission media as well as extending more advanced applications with versatile spatial modes in fibers would be of great interest.

Data Availability

All the findings of this study are available in the main text. The raw data are available from the corresponding author upon reasonable request.

Acknowledgments

This work was supported by the National Natural Science Foundation of China (Grant Nos. 62125503 and 62261160388), the National Key R&D Program of China (Grant No. 2019YFB2203604), the Key R&D Program of Hubei Province of China (Grant Nos. 2020BAB001 and 2021BAA024), the Shenzhen Science and Technology Program (Grant No. JCYJ20200109114018750), and the Innovation Project of Optics Valley Laboratory (Grant No. OVL2021BG004). J.W. developed the concept and conceived the experiment. J.W. and H.W. performed the theoretical analyses. Z.M. and S.R. provided the air-core fiber and technical supports. H.W. and J.A. constructed the experiment. H.W. and J.W. acquired the experimental data and carried out the data analyses. J.W., H.W., and Z.M. contributed to writing this paper. J.W. finalized this paper and supervised the project. The authors declare no competing financial interests.

References

- D. J. Richardson, J. M. Fini, and L. E. Nelson, “Space-division multiplexing in optical fibres,” *Nat. Photonics* **7**, 354–362 (2013).
- R. G. H. Van Uden et al., “Ultra-high-density spatial division multiplexing with a few-mode multicore fibre,” *Nat. Photonics* **8**, 865–870 (2014).
- G. Li et al., “Space-division multiplexing: the next frontier in optical communication,” *Adv. Opt. Photonics* **6**, 413–487 (2014).
- R. Ryf et al., “Mode-division multiplexing over 96 km of few-mode fiber using coherent 6×6 MIMO processing,” *J. Lightwave Technol.* **30**, 521–531 (2012).
- D. Soma et al., “257-Tbit/s weakly coupled 10-mode C+L-band WDM transmission,” *J. Lightwave Technol.* **36**, 1375–1381 (2018).
- J. Li et al., “Terabit mode division multiplexing discrete multitone signal transmission over OM2 multimode fiber,” *IEEE J. Sel. Top. Quantum Electron.* **26**, 4501308 (2020).
- F. Yaman et al., “Long distance transmission in few-mode fibers,” *Opt. Express* **18**, 13250–13257 (2010).
- L. Zhu et al., “Encoding/decoding using superpositions of spatial modes for image transfer in km-scale few-mode fiber,” *Opt. Express* **24**, 16934–16944 (2016).
- D. Soma et al., “10.16-peta-b/s dense SDM/WDM transmission over 6-mode 19-core fiber across the C+L band,” *J. Lightwave Technol.* **36**, 1362–1368 (2018).
- G. Milione et al., “ 4×20 Gbit/s mode division multiplexing over free space using vector modes and a q -plate mode (de)multiplexer,” *Opt. Lett.* **40**, 1980–1983 (2015).
- Y. Zhao and J. Wang, “High-base vector beam encoding/decoding for visible-light communications,” *Opt. Lett.* **40**, 4843–4846 (2015).
- L. Wang et al., “Linearly polarized vector modes: enabling MIMO-free mode-division multiplexing,” *Opt. Express* **25**, 11736–11749 (2017).
- J. Liu et al., “Direct fiber vector eigenmode multiplexing transmission seeded by integrated optical vortex emitters,” *Light Sci. Appl.* **7**, 17148 (2018).
- J. Zhang et al., “Fiber vector eigenmode multiplexing based high capacity transmission over 5-km FMF with Kramers–Kronig receiver,” *J. Lightwave Technol.* **39**, 4932–4938 (2021).
- N. Bozinovic et al., “Terabit-scale orbital angular momentum mode division multiplexing in fibers,” *Science* **340**, 1545–1548 (2013).
- A. D. Wang et al., “Demonstration of hybrid orbital angular momentum multiplexing and time-division multiplexing passive optical network,” *Opt. Express* **23**, 29457–29466 (2015).
- A. D. Wang et al., “Characterization of LDPC-coded orbital angular momentum modes transmission and multiplexing over a 50-km fiber,” *Opt. Express* **24**, 11716–11726 (2016).
- J. Wang, “Advances in communications using optical vortices,” *Photonics Res.* **4**, B14–B28 (2016).
- S. Chen et al., “Full-duplex bidirectional data transmission link using twisted lights multiplexing over 1.1-km orbital angular momentum fiber,” *Sci. Rep.* **6**, 38181 (2016).
- J. Wang, “Data information transfer using complex optical fields: a review and perspective,” *Chin. Opt. Lett.* **15**, 030005 (2017).
- K. Ingerslev et al., “12 mode, WDM, MIMO-free orbital angular momentum transmission,” *Opt. Express* **26**, 20225–20232 (2018).
- L. Zhu et al., “18 km low-crosstalk OAM + WDM transmission with 224 individual channels enabled by a ring-core fiber with large high-order mode group separation,” *Opt. Lett.* **43**, 1890–1893 (2018).
- G. X. Zhu et al., “Scalable mode division multiplexed transmission over a 10-km ring-core fiber using high-order orbital angular momentum modes,” *Opt. Express* **26**, 594–604 (2018).
- J. Wang, “Twisted optical communications using orbital angular momentum,” *Sci. China Phys. Mech.* **62**, 034201 (2019).
- P. Gregg et al., “Enhanced spin orbit interaction of light in highly confining optical fibers for mode division multiplexing,” *Nat. Commun.* **10**, 4707 (2019).
- S. Chen et al., “OAM mode multiplexing in weakly guiding ring-core fiber with simplified MIMO-DSP,” *Opt. Express* **27**, 38049–38060 (2019).
- H. Y. Wang et al., “Low-loss orbital angular momentum ring-core fiber design, fabrication and characterization,” *J. Lightwave Technol.* **38**, 6327–6333 (2020).
- J. Zhang et al., “Mode division multiplexed transmission of WDM signals over 100-km single-span OAM fiber,” *Photonics Res.* **8**, 1236–1242 (2020).
- L. Zhu et al., “Orbital angular momentum mode groups multiplexing transmission over 2.6-km conventional multi-mode fiber,” *Opt. Express* **25**, 25637–25645 (2017).
- S. Chen and J. Wang, “Theoretical analyses on orbital angular momentum modes in conventional graded-index multimode fibre,” *Sci. Rep.* **7**, 3990 (2017).
- A. D. Wang et al., “Directly using 8.8-km conventional multimode fiber for 6-mode orbital angular momentum multiplexing transmission,” *Opt. Express* **26**, 10038–10047 (2018).
- J. Wang, S. Chen, and J. Liu, “Orbital angular momentum communications based on standard multimode fiber [Invited paper],” *APL Photonics* **6**, 060804 (2021).
- L. Wang et al., “Deep learning based recognition of different mode bases in ring-core fiber,” *Laser Photonics Rev.* **14**, 2000249 (2020).
- E. Ip et al., “SDM transmission of real-time 10GbE traffic using commercial SFP+ transceivers over 0.5 km elliptical-core few-mode fiber,” *Opt. Express* **23**, 17120–17126 (2015).
- S. Chen and J. Wang, “Fully degeneracy-lifted bow-tie elliptical ring-core multi-mode fiber,” *Opt. Express* **26**, 18773–18782 (2018).
- L. Wang et al., “MDM transmission of CAP-16 signals over 1.1-km elliptical-core few-mode fiber in passive optical networks,” *Opt. Express* **25**, 22991–23002 (2017).
- H. Yan et al., “Design of PANDA ring-core fiber with 10 polarization-maintaining modes,” *Photonics Res.* **5**, 1–5 (2017).

38. S. Chen and J. Wang, "Design of PANDA-type elliptical-core multimode fiber supporting 24 fully lifted eigenmodes," *Opt. Lett.* **43**, 3718–3721 (2018).
39. J. Zhao et al., "Polarization-maintaining few mode fiber composed of a central circular-hole and an elliptical-ring core," *Photonics Res.* **5**, 261–266 (2017).
40. S. Chen and J. Wang, "Photonic crystal fibers supporting fully separated eigenmodes," *Opt. Lett.* **44**, 3046–3049 (2019).
41. P. Gregg, P. Kristensen, and S. Ramachandran, "Conservation of orbital angular momentum in air-core optical fibers," *Optica* **2**, 267–270 (2015).
42. P. Gregg, P. Kristensen, and S. Ramachandran, "13.4 km OAM state propagation by recirculating fiber loop," *Opt. Express* **24**, 18938–18947 (2016).
43. Z. Ma et al., "Robustness of OAM fiber modes to geometric perturbations," in *Conf. Lasers and Electro-Opt. (CLEO)*, p. SW3K.1 (2018).
44. Z. Ma and S. Ramachandran, "Propagation stability in optical fibers role of path memory and angular momentum," *Nanophotonics* **10**, 209–224 (2021).
45. A. Bjarklev, "Microdeformation losses of single-mode fibers with step-index profiles," *J. Lightwave Technol.* **4**, 341–346 (1986).
46. R. Y. Chiao and Y.-S. Wu, "Manifestations of Berry's topological phase for the photon," *Phys. Rev. Lett.* **57**, 993–996 (1986).
47. A. Tomita and R. Y. Chiao, "Observation of Berry's topological phase by use of an optical fiber," *Phys. Rev. Lett.* **57**, 937–940 (1986).
48. K. Y. Bliokh, "Geometrical optics of beams with vortices Berry phase and orbital angular momentum Hall effect," *Phys. Rev. Lett.* **97**, 043901 (2006).
49. G. C. G. Berkhout et al., "Efficient sorting of orbital angular momentum states of light," *Phys. Rev. Lett.* **105**, 153601 (2010).
50. M. Mirhosseini et al., "Efficient separation of the orbital angular momentum eigenstates of light," *Nat. Commun.* **4**, 2781 (2013).
51. C. Wan, J. Chen, and Q. Zhan, "Compact and high-resolution optical angular momentum sorter," *APL Photonics* **2**, 031302 (2017).
52. Y. Wen et al., "Spiral transformation for high-resolution and efficient sorting of optical vortex modes," *Phys. Rev. Lett.* **120**, 193904 (2018).
53. N. K. Fontaine et al., "Laguerre–Gaussian mode sorter," *Nat. Commun.* **10**, 1865 (2019).
54. J. C. Fang et al., "Optical orbital angular momentum multiplexing communication via inverse-designed multi-phase plane light conversion," *Photonics Res.* **10**, 2015–2023 (2022).
55. M. B. Shemirani et al., "Principal modes in graded-index multimode fiber in presence of spatial- and polarization-mode coupling," *J. Lightwave Technol.* **27**, 1248–1261 (2009).
56. J. Carpenter, B. J. Eggleton, and J. Schröder, "Observation of Eisenbud–Wigner–Smith states as principal modes in multimode fibre," *Nat. Photonics* **9**, 751–757 (2015).
57. J. Wang et al., "Orbital angular momentum and beyond in free-space optical communications," *Nanophotonics* **11**, 645–680 (2022).
58. L. Zhu, A. D. Wang, and J. Wang, "Free-space data-carrying bendable light communications," *Sci. Rep.* **9**, 14969 (2019).
59. R. Z. Zhang et al., "Turbulence-resilient pilot-assisted self-coherent free-space optical communications using automatic optoelectronic mixing of many modes," *Nat. Photonics* **15**, 743–750 (2021).
60. Z. Y. Zhu et al., "Compensation-free high-dimensional free-space optical communication using turbulence-resilient vector beams," *Nat. Commun.* **12**, 1666 (2021).
61. I. Nape et al., "Revealing the invariance of vectorial structured light in complex media," *Nat. Photonics* **16**, 538–546 (2022).
62. L. Fang et al., "Spin-orbit mapping of light," *Phys. Rev. Lett.* **127**, 233901 (2021).
63. A. P. Greenberg, G. Prabhakar, and S. Ramachandran, "High resolution spectral metrology leveraging topologically enhanced optical activity in fibers," *Nat. Commun.* **11**, 5257 (2020).
64. J. Demas et al., "Intermodal nonlinear mixing with Bessel beams in optical fiber," *Optica* **2**, 14–17 (2015).
65. D. Stellinga et al., "Time-of-flight 3D imaging through multimode optical fibers," *Science* **374**, 1395–1399 (2021).
66. Z. Wan et al., "Remote and robust measurement of the angular velocity vector based on vectorial Doppler effect using air-core optical fiber," *Research* **2022**, 9839502 (2022).
67. J. Liu et al., "Multidimensional entanglement transport through single-mode fiber," *Sci. Adv.* **6**, eaay0837 (2020).
68. Q. K. Wang et al., "High-dimensional quantum cryptography with hybrid orbital-angular-momentum states through 25 km of ring-core fiber: a proof-of-concept demonstration," *Phys. Rev. Appl.* **15**, 064034 (2021).

Jian Wang received his PhD in physical electronics from Wuhan National Laboratory for Optoelectronics, Huazhong University of Science and Technology, China, in 2008. He worked as a postdoctoral research associate in the Optical Communications Laboratory at the University of Southern California, United States, from 2009 to 2011. Currently, he is a professor at Wuhan National Laboratory for Optoelectronics, Huazhong University of Science and Technology, China. He is vice director of Wuhan National Laboratory for Optoelectronics, Huazhong University of Science and Technology, China. He was elected as an OPTICA fellow (formerly OSA fellow) in 2020, and SPIE fellow in 2022. He leads the Multi-dimensional Photonics Laboratory. His research interests include optical communications, optical signal processing, silicon photonics, photonic integration, OAM, and structured light.

Biographies of the other authors are not available.